# Recent climatological trend of the Saharan heat low and its impact on the West African climate

Christophe Lavaysse, Cyrille Flamant, Amato T. Evan, Serge Janicot, Marco Gaetani

Clim Dyn
DOI 10.1007/s00382-015-2847-z

# Recent climatological trend of the Saharan heat low and its impact on the West African climate

**Christophe Lavaysse[1] · Cyrille Flamant[2] · Amato Evan[3] · Serge Janicot[4] · Marco Gaetani[2]**

Received: 22 June 2015 / Accepted: 20 September 2015


**Abstract** The Saharan heat low (SHL) plays a pivotal role in the West African monsoon system in spring and summer. The recent trend in SHL activity has been analysed using two sets of numerical weather prediction (NWP) model reanalyses and Atmospheric Models Intercomparison Project simulations from 15 climate models performed in the framework of the 5th Coupled Models Intercomparison Project (CMIP5) exercise. A local increase of temperature in the Sahara during the 90s is found in the two sets of NWP models temperature. This increase is stronger within the SHL region than over the surrounding areas. Using different temporal filters (under 25 days, 25–100 days and above 300 days), we show that this is accompanied by a slight but widespread increase of temperature, and a change in the filtered signal under 25 days during the transition period of the 90s. We also show that SHL pulsations occurring at different time scales impact the West Africa climate on a variety of spatial scales, from the regional scale (for the high band pass) to the synoptic scale (for the low band pass signal). Despite a large variability in the temporal trends for 15 climate models from the CMIP5 project, the warming trend in the 90s is observed in the models ensemble mean. Nevertheless, large discrepancies are found between the NWP models reanalyses and the climate model simulations regarding the spatial and temporal evolutions of the SHL as well as its impact on West African climate at the different time scales. These comparisons also reveal that climate models represent the West African monsoon interactions with SHL pulsations quite differently. We provide recommendations to use some of them depending on the time scales of the processes at play (synoptic, seasonal, interannual) and based on key SHL metrics (location, mean intensity, global trend, interaction with the West African monsoon dynamics).

**Keywords** West African monsoon · Heat low · Precipitation · Climate change · Numerical weather prediction model reanalyses, climate models

## 1 Introduction

The West African heat low is the thermal response of the lower troposphere over the northern African continent to the seasonal surface warming (Lavaysse et al. 2009). In summertime, this low pressure is located over the Sahara, and hence termed Saharan heat low (SHL), and has been identified as a major component of the West African monsoon (WAM) system (Sultan and Janicot 2003; Parker et al. 2005; Peyrillé and Lafore 2007; Lavaysse et al. 2009) and a driver of precipitation over the Sahel (Lavaysse et al. 2010a; Evan et al. 2015). As such, the SHL interacts with many key features of the WAM. In the lower troposphere, the cyclonic

This paper is a contribution to the special issue on West African climate decadal variability and its modeling, consisting of papers from the West African Monsoon Modeling and Evaluation (WAMME) and the African Multidisciplinary Monsoon Analyses (AMMA) projects, and coordinated by Yongkang Xue, Serge Janicot, and William Lau.

✉ Christophe Lavaysse
christophe.lavaysse@jrc.ec.europa.eu

[1] European Commission, Joint Research Centre, TP124, 21027 Ispra, VA, Italy

[2] CNRS and UVSQ, UMR 8190 LATMOS, UPMC Univ Paris 06, Sorbonne Universités, 75005 Paris, France

[3] Scripps Institution of Oceanography, University of California, San Diego, La Jolla, CA, USA

[4] LOCEAN, UPMC Univ Paris 06 and IRD, Paris, France

Published online: 01 October 2015

circulation generated by an intense SHL tends to reinforce the southwesterly monsoon flow along its eastern flank and the northeasterly Harmattan flow along the western flank. Parker et al. (2005) suggested that such circulation is likely to enhance the probability of moist convection and cloud cover poleward of the depression center. In the mid-troposphere, the anticyclonic circulation associated with the diverging flow at the top of the SHL contributes to the maintenance of the African Easterly Jet (AEJ) and modulates its intensity (Thorncroft and Blackburn 1999). An intensification of the AEJ is indeed observed during strong phases of the SHL, associated with high temperatures in the Saharan boundary layer (Lavaysse et al. 2010b). At the intra-seasonal scale, the pulsations of the SHL, and of the WAM system in general, are connected to the westward propagation of African Easterly Waves (AEWs) and the alternation of moist/cool advection and hot/dry lower tropospheric air masses linked to the southerly and northerly sectors of the AEWs, the former leading to an increase in convective activity over the Sahel (Lavaysse et al. 2010b).

The WAM system is also influenced by more global phenomena occurring at longer timescales, such as the quasi-biweekly zonal dipole of convection (Mounier et al. 2008) with a mean periodicity of about 14 days, or the specific 15-day periodicity mode of convection related to equatorial Rossby waves (Janicot et al. 2009). The latter is one of the most important mode of variability of convection over the Sahel (Janicot et al. 2011).

The Madden–Julian Oscillation (MJO) also plays a key role over West Africa (Matthews 2004) in explaining the 25–90-day mode of variability of convection (Mohino et al. 2012); here, the authors suggested that equatorial dry Kelvin waves and dry Rossby waves could link the MJO in the Indian sector and the African MJO mode. This westward propagation of convection anomalies is also preceded by the development of low geopotential areas associated with enhanced convection over northern India.

At longer time scales, the WAM shows significant modifications, especially in terms of temperature, precipitation. The multidecadal precipitation variability in the twentieth century is dominated by the Global Ocean sea surface temperature (SST). The Tropical Ocean warming, associated with global warming and positive phases of the interdecadal Pacific oscillation (IPO), favours dry conditions in the Sahel, through the inhibition of the tropical convection (Lu and Delworth 2005; Villamayor and Mohino 2015). On the other hand, positive phases of the Atlantic multidecadal variability (AMV), and the related northward displacement of the intertropical convergence zone (ITCZ), favour precipitation in the Sahel (Ting et al. 2009; Mohino et al. 2011). The recent variability of the WAM at inter-decadal scales has been studied by Li et al. (2012), who observed a strengthening of the monsoon from 1998, concomitant with an increase of precipitation in the −20°W to 0°E longitudinal band over Sahel. They explained this increase by an intensification of the vertical ascending motion over the WAM region and enhanced divergence in the upper troposphere. Also, they observed an increase of the southwestly (eastly) winds in the lower (upper) levels over the WAM region associated with an intensification of column integrated moisture flux convergence. The authors explain the recent strengthening by the north Pacific SST, while the relationship with the south Pacific and north Atlantic variations are not significant.

Cook and Vizy (2015) showed that the annual warming trend in the Sahara exceeds the global and the tropical warming by a factor of 2.5 and 4, respectively. They explained this difference by the increase of the upward longwave radiation from the surface. Even if, as discussed by Lavaysse (2015), the linear trend assumption used by Cook and Vizy (2015) can partially mislead these trends, these enhanced trends, in turn, having an impact on the monsoon circulation and on the precipitation over the Sahel. Evan et al. (2015) analyzed the recent recovery from the Sahelian drought of the 1980s. They examined the role of the SHL and suggest the trends were forced by anomalous nighttime long wave heating of the surface by water vapour. They find a positive relationship between Sahel rainfall and Saharan surface temperatures. Finally they demonstrated that the recovery in Sahelian rainfall is consistent with an intensification of the SHL.

These climatological trends highlight the recent modifications of the WAM and their potential consequences on precipitation over Sahel. This is particularly important to understand the recent studies of the WAM, as well as future trends. In the Coupled Model Intercomparison Project phase 5 (CMIP5) exercise, under the Representative Concentration Pathway (RCP4.5 and RCP8.5) scenarii from the 5th Assessment Report of the GIEC, some model display a decrease of rainfall in the Western part of the Sahel and an increase on the eastern part and a local increase of temperature over the Sahara (Monerie et al. 2012; Lee and Wang 2014).

Evan et al. (2015) have shown that when forced by SST alone, most state-of-the-art climate models involved in CMIP5 do not reproduce a statistically significant upward trend in Sahelian precipitation over the last 30 years and the authors stress that the models with a significant upward trend in rainfall seem to achieve this result for disparate reasons. Roehrig et al. (2013) have highlighted that the CMIP5 SST-imposed models partially succeed in capturing the recent partial recovery of monsoon rainfall. But as observed for the decadal trend from each individual model in Fig. 3a of Roehrig et al. (2013), the uncertainties are important. These uncertainties limit the interest of the use of precipitation fields in climate models over Sahel, for both historical simulations and projections.

**Table 1** Characteristics of the 15 AMIP simulation models used in this study

| Centre | Models | Horizontal resolution | Vertical levels | References |
|---|---|---|---|---|
| Norwegian Climate Centre | NorESM1-M (NCC) | 1.9 × 2.5 | 26 | Kirkevåg et al. (2008) |
| Meteorological Research Institute | MRI-AGCM3.2H (MRI) | 0.56 × 0.56 | 64 | Mizuta et al. (2012) |
| Max Planck Institute for Meteorology | MPI-ESM-LR (MPI) | 1.875 × 1.875 | 47 | http://www.mpimet.mpg.de/en/science/models/mpi-esm.html |
| Beijing Climate Center | bcc-csm1 (BCC) | 2.8 × 2.8 | 26 | Wu et al. (2010) |
| National Center for Atmospheric Research | CCSM4 (NCAR) | 0.9 × 1.25 | 26 | Neale et al. (2013) |
| Centre National de Recherches Metorologiques | CNRM-CM5 (CNRM) | 1.4 × 1.4 | 31 | Voldoire et al. (2013) |
| Institute of Numerical Mathematics | INM-C4 | 1.5 × 2.5 | 21 | Volodin et al. (2010) |
| Institut Pierre-Simon Laplace | IPSLA (IPSLA) | 1.895 × 3.75 | 39 | Dufresne et al. (2013) |
| Institut Pierre-Simon Laplace | IPSLB (IPSLB) | 1.25 × 2.5 | 39 | Dufresne et al. (2013) |
| European Consortium | EC-EARTH (ICHEC) | 1.125 × 1.125 | 62 | Hazeleger et al. (2010) |
| Commonwealth Scientific and Industrial Research Organisation | CSIRO-Mk3.6.0 (CSIRO) | 1.875 × 1.875 | 18 | Rotstayn et al. (2010) |
| Canadian Centre for Climate Modelling and Analysis | CanAM4 (CCCma) | 1.875 × 1.875 | 35 | http://www.ec.gc.ca/ccmac-cccma |
| Met Office Hadley Centre | HadGEM2-A (HadGEM2) | 1.25 × 1.875 | 38 | Collins et al. (2008) |
| National Oceanic and Atmospheric Administration | GFDL-HIRAM-C180 (GFDL180) | 0.5 × 0.5 | 32 | Donner et al. (2011) |
| Geophysical Fluid Dynamics Laboratory | GFDL-HIRAM-C360 (GFDL360) | 0.25 × 0.25 | 32 | Donner et al. (2011) |

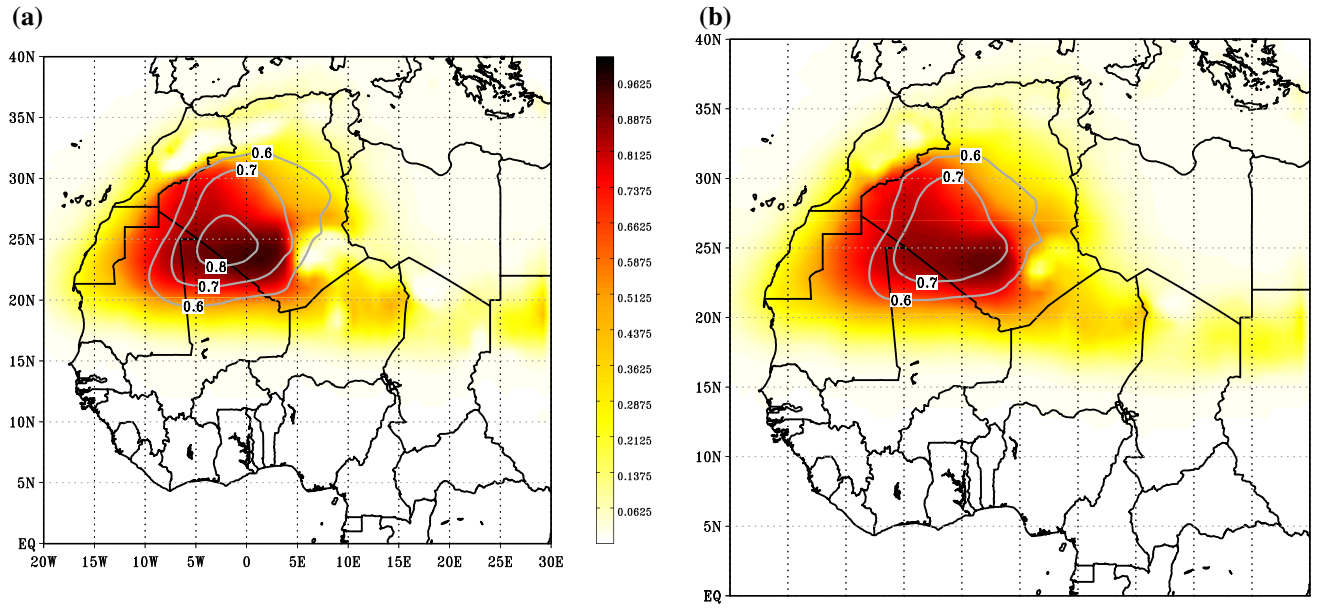


**Fig. 1** Mean occurrence probability of the heat low detection during the summer season (i.e. from 20 June to 17 September) from 1979 to 2012 using the low level atmospheric thickness (*left panel*) and the 850 hPa temperature field (*right panel*) provided by ERA-Interim. *Thin contours* indicate the correlation between the temperature of each grid point and the intensity of the SHL by the method developed in Lavaysse et al. (2009)

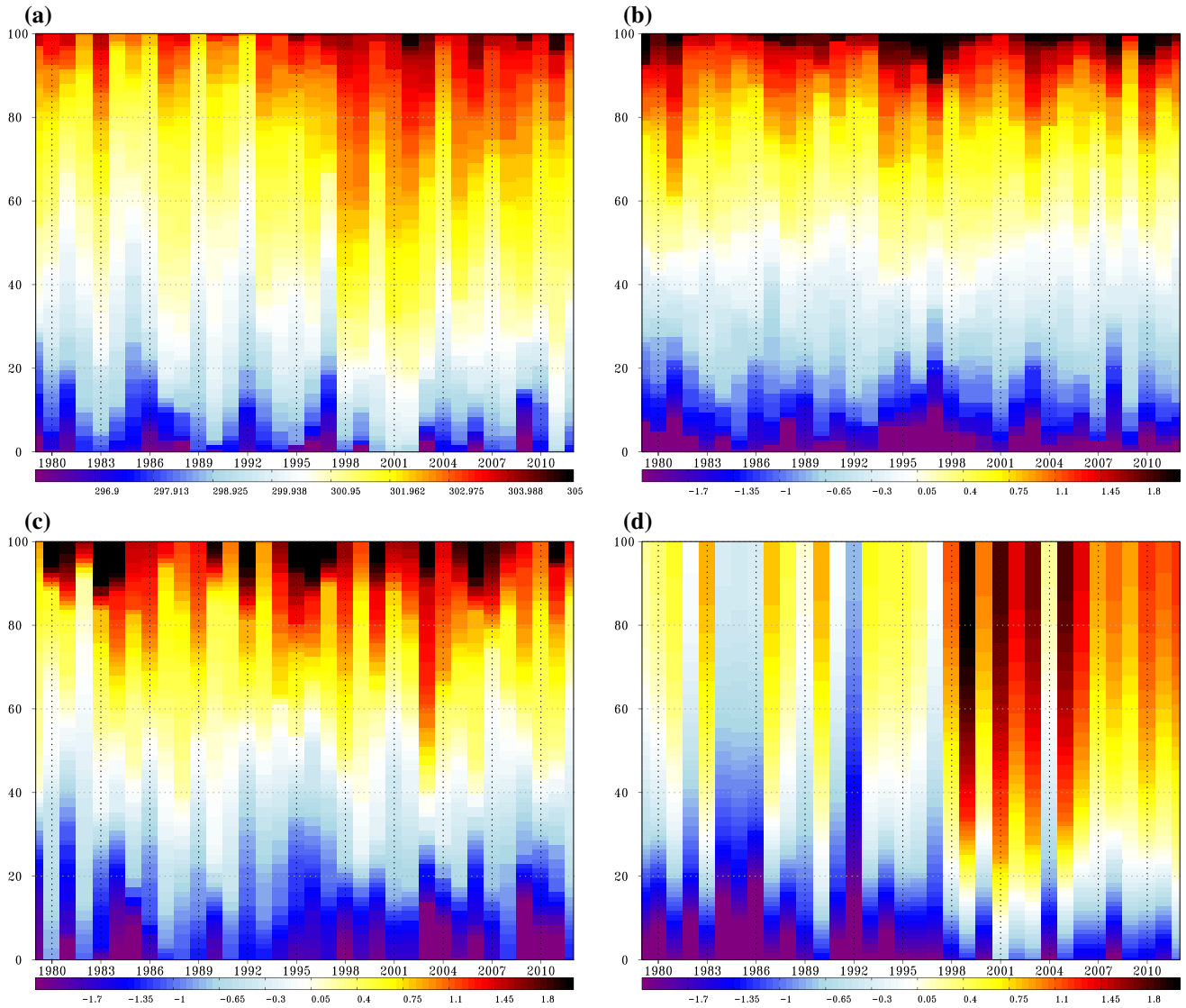


**Fig. 2** Yearly distribution from the lowest to the largest value (y-axis), of the SHL temperature in summer defined between the 20 June and 17 September from 1979 to 2012 (x-axis) using the unfiltered data of ERAI (**a**), using the high band pass filter (lower than 25 days, **b**), filtered in the 25–100-day band (**c**), and with a low band pass filter (define larger than 300 days, **d**). The temperature have been ranked each year from the lowest to the largest values (in degree)

These studies highlight the importance to better understand the recent changes in the WAM key components observed at decadal scales and their link with changes occurring at much shorter time scales. This could be important to identify predictors and better understand the underlying processes. This is especially relevant over West Africa due to the high variability of the seasonal accumulated precipitation over a semi-arid area where the resilience of the populations to climate variability is significantly low. Moreover, the recent evolution of temperature fields (which is better represented than precipitation in the climate models) and the trend simulated over West Africa for the next century show an enhanced temperature trend over the Sahel (Vizy et al. 2013).

The SHL is a reliable indicator of the regional and large scale forcings impacting the WAM such as AEWs, MJOs, mid-latitude circulation (Lavaysse et al. 2010b). The aim of this study is to analyze the impact of the SHL on its environment at the relevant time scales based on the SHL characteristic variability modes highlighted above, and to identify which WAM climatological feature is most sensible to the SHL and at which time scales. This detection/attribution approach will first be applied to reanalyses to define basic links between the SHL and WAM features. The approach will then be applied to 15 CMIP5 models Atmospheric Model Intercomparison Project (AMIP) simulations to determine whether these links are robust features in the AMIP simulations from state-of-the-art climate models.

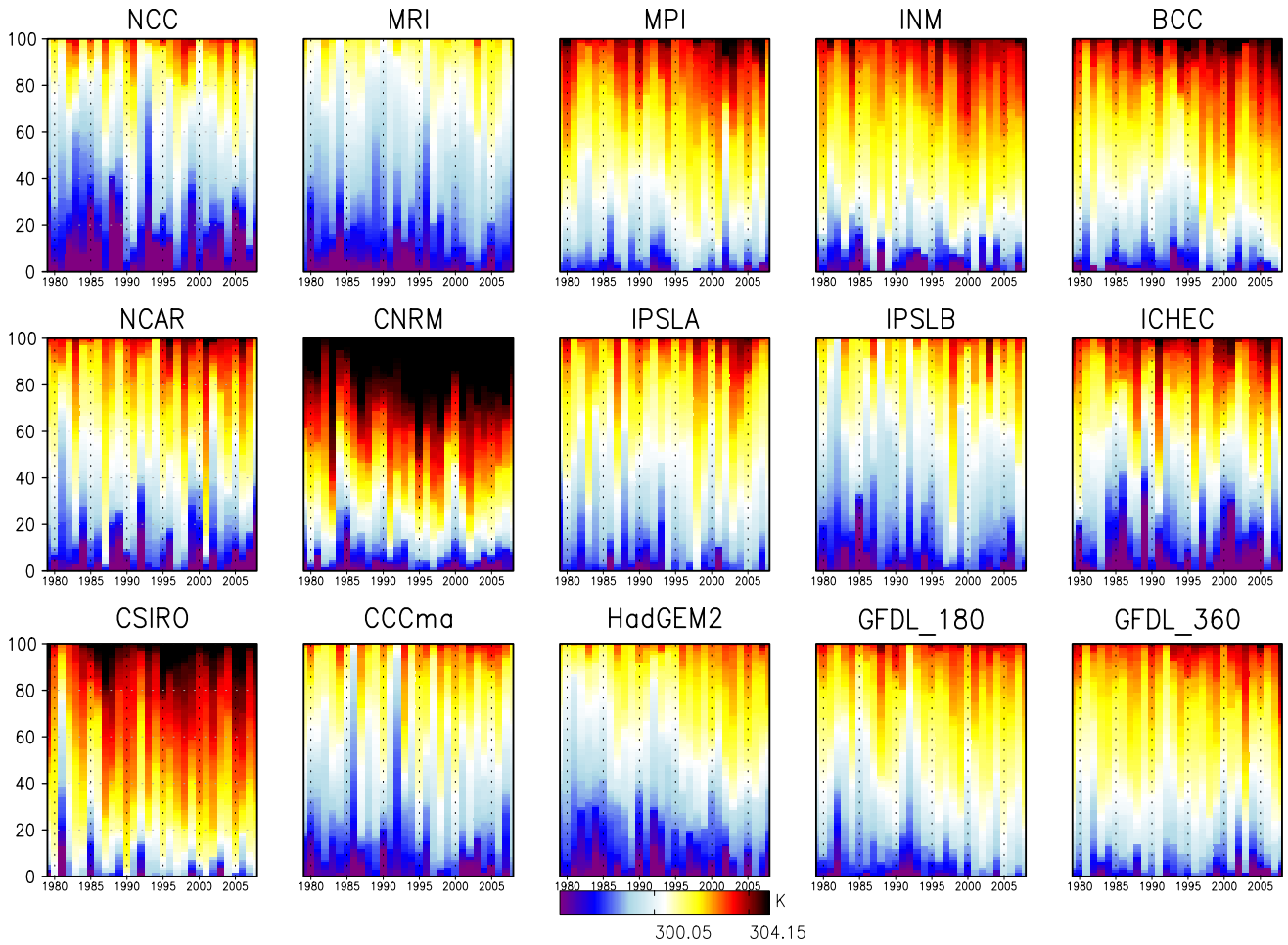


**Fig. 3** Same as Fig. 2a but by using the 15 climate models

This AMIP experiment was chosen based on the results from Roehrig et al. (2013) showing that SST-forced runs better represent the partial recovery of precipitation. This is a key issue to address prior to attempting an analysis of the influence of the SHL on the WAM in CMIP5 projections.

## 2 Data and methods

### 2.1 Numerical weather prediction models reanalyses

We focus on the period of maximum activity of the heat low, i.e. when it is located over the Sahara during the summer, and it is referred as SHL. Following Lavaysse et al. (2009), this period starts in average on 20 June and finishes on 17 September, based on analysis of 30 years of European Center for Medium-range Weather Forecasts (ECMWF) reanalyses.

Two sets of reanalysis have been analyzed for the period from 1979 to 2012. The first reanalysis is the ECMWF ERA-Interim reanalyses (Dee et al. 2011) that has already been used extensively to study the WAM. It has been highlighted that ERA-Interim reanalyses correctly represents the main monsoon features and their characteristic modes of variability at both seasonal and intra-seasonal time scales (e.g. Lavaysse et al. 2009). A second set of reanalyses from the US National Center for Environmental Predictions (NCEP2 reanalyses, Kalnay et al. 1996) has been used to assess the significance of the results obtained with ECMWF reanalyses.

In the following, we use the wind fields at 925 and 700 hPa which allow characterizing the main synoptic features of the WAM system. The 925 hPa wind field is used to determine the intensity of the monsoon flow and the Harmattan winds and the location of the cyclonic circulation associated with the SHL. The 700 hPa winds are used to characterize the AEJ and AEWs. In Lavaysse et al. (2009), the method to characterize the SHL was based on the thickness of the low levels atmospheric layer computed from the difference of geopotential heights at 700 and 925 hPa. They have shown that this thickness is also directly related to the average temperature in the 925–700 hPa layer and

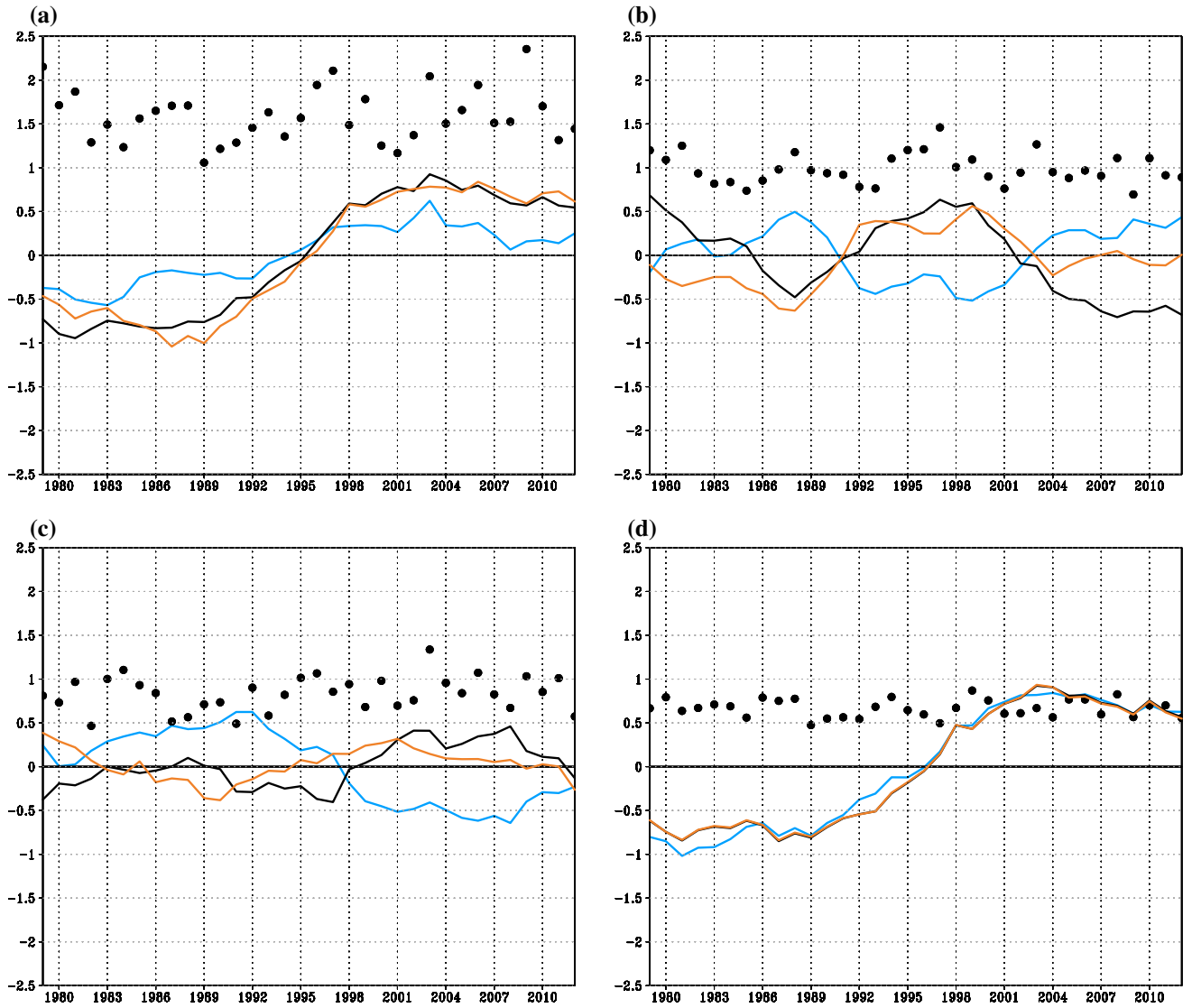


**Fig. 4** Temporal evolution of the standardized quantile 10 (*blue lines*), quantile 90 (*red lines*) and of the median of the SHL intensity (*black lines*) for each year from 1979 to 2012 using the unfiltered signal of ERAI (**a**), the high band pass filtered signal (**b**), the 25–100-day filtered signal (**c**), and the low band pass filtered signal (**d**). *Black points* indicate the yearly standard deviation of each signal

particularly well correlated with the 850 hPa temperature field. Based on this, and in order to simplify the data collection from Climate models, the temperature fields at 850 hPa will be used to assess the intensity of the SHL. Daily averaged temperature and wind fields, calculated from the six hourly fields, are used, which yield a horizontal grid size 0.75° × 0.75° and 2.5° × 2.5° for ERAI and NCEP2, respectively.

### 2.2 Climate models simulations

The simulations performed by an ensemble of General Circulation Models (GCMs) as part of CMIP5 and used in the present study are listed in Table 1. They were made available via the Earth System Grid (ESG; http://cmip-pcmdi.llnl.gov/cmip5/index.html) data archive. The CMIP5 experiments are described in Taylor et al. (2012). As we later show a more detailed evaluation of the CMIP5 AMIP simulations, the table also includes grid information for the atmospheric component of these models. Based on Roehrig et al. (2013), the SST-forced runs, most relevant to study the African Monsoon, are used. Simulations are performed by prescribing observed SST and sea ice for the period 1979 to the present. The same meteorological fields as in the reanalyses have been used.

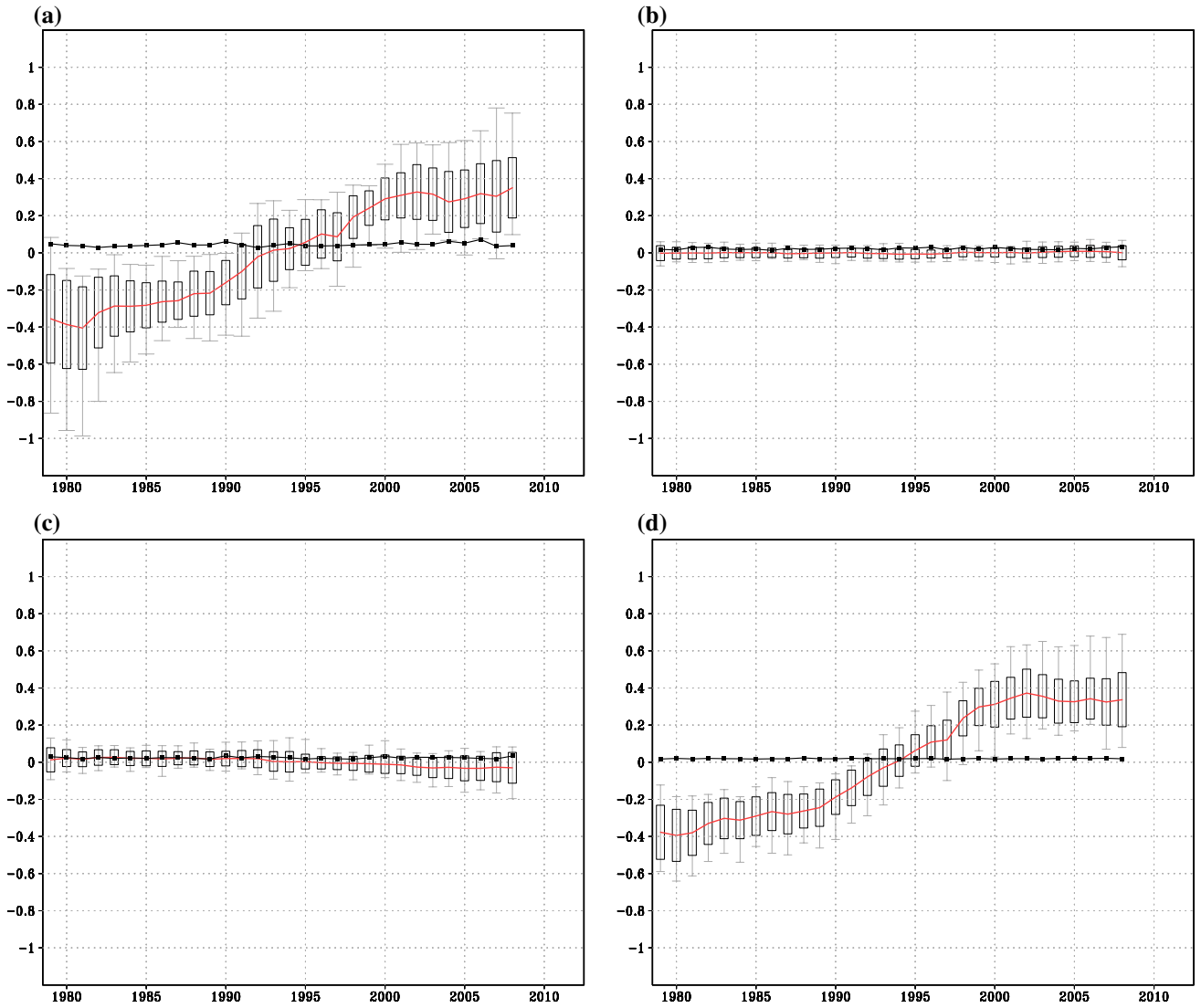


**Fig. 5** Spread and average (*barb* and *red lines* respectively) of the 15 climate models for each year from 1979 to 2012 using the unfiltered signal (**a**), the high band pass filtered signal (**b**), the 25–100-day filtered signal (**c**), and the low band pass filtered signal (**d**). *Black lines* indicate the spread of the 15 climate models

### 2.3 Precipitation observations

Version 1.2 of the Global Precipitation Climatology Project (GPCP, Huffman et al. 2001) data set has been used to provide the large scale pattern of precipitation over West Africa. The daily accumulated precipitation is computed from the GPCP Global Merge Development Centre and available on a 1° global grid. Data from geostationary satellites as well as infrared and passive microwave instruments on-board polar orbiting platforms, together with sounding observations have been merged to estimate daily rainfall from 1986 to the present. It is worth noting that the product has been validated over West Africa (Nicholson et al. 2003).

### 2.4 Methodology

In previous studies, the SHL position estimated based on an Eulerian approach (e.g. Lavaysse et al. 2009) was shown to be stable over the Saharan area and the intra-seasonal mode of variability of the Sahara temperature to be well correlated with the pulsation of the area defined as the SHL region. In order to simplify the multi-model analysis we shall analyze the temporal variability of the temperature over the Sahara (a proxy of the temporal variability of the SHL intensity) in the domain where Lavaysse et al. (2009) detected the presence of the SHL with an occurrence probability larger than 0.75 (i.e. between 7°W and 5°E and from 20°N to 30°N, see Fig. 1).

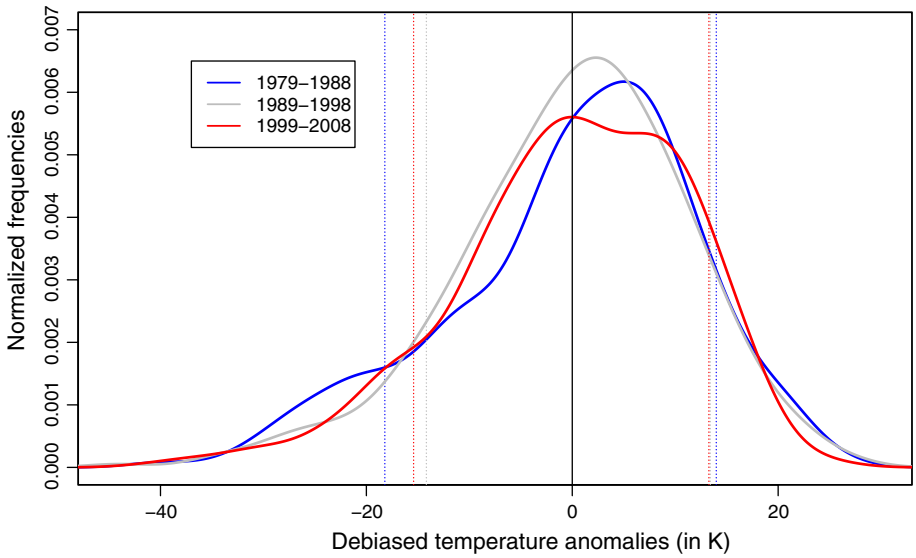


**Fig. 6** Distribution of the normalized frequencies of the debiased SHL activity (depicted by the 850 hPa temperature using ERAI) for the period 1980–1990 (*red line*), 1991–2000 (*green line*) and 2001–2010 (*blue line*). The bias is assessed in relation to the mean SHL intensity during the respective periods. *Dotted lines* indicate the last quantiles of each distribution

As shown previously (Lavaysse et al. 2010b; Chauvin et al. 2010; Roehrig et al. 2011), the mode of variability of the SHL detected with a periodicity lower than 25 days is strongly related to convective activity and precipitation over the Sahel. To focus more specifically on these pulsations associated with synoptic components, we apply a high-pass filter with a cutoff frequency of 25 days to the data sets (temperature and wind fields from both the reanalyses and the climate models as well as observed precipitation fields). A second filter, a band-pass filter passing frequencies between 25 and 100 days, allows to focus on several variability modes occurring at the global scale that influence the convection over West Africa, such as the MJO. A third filter, a last low-pass filter with a cutoff frequency of 300 days, serves to characterize the seasonal and multi-years evolution of the fields under scrutiny. We have also tested the decomposition between the seasonal cycle (with a band pass filter from 300 to 400 days) and a low pass filter to select only the long-term trend (with a cutoff frequency of 730 days). We found very similar results in term of impacts. The only differences were the intensities of the signals (stronger for the seasonal cycle) and the long term trends (stronger for the low-pass signal). That is why we have used a low pass filter with a cutoff at 300 days. Note that in order to avoid boundary effects, and to highlight the climatological trend, filtering is applied to complete data sets (i.e. for the period from 1979 to 2012, not just the summer months).

## 3 Recent evolution of the SHL intensity

### 3.1 Temporal trend

To focus on the recent trend of the SHL characteristics, the distribution of daily SHL intensities during the summer season, defined as the period where the heat low is located in his Saharan location (i.e. from 20 June to 17 September), of each year has been analyzed. The SHL intensities are sorted from the coldest to the warmest temperature for each year for the period 1979–2012 (Fig. 2). Based on the unfiltered temperature from the ERAI reanalyses (Fig. 2a), the entire temperature range seems to increase from 1979 to 2012. This increase is the strongest in the middle of the 90s. For example, the occurrence of the temperature larger than 303 K increased from around 10 % in the 80s to around 30 % from the 90s.

The same trend is analyzed using temperature fields from the climate models (Fig. 3). First, the model bias can be assessed. The CNRM and CSIRO models present a strong warm bias in the SHL region, whereas MRI and HadGEM2 exhibit a cold bias, with respect to reanalyses. All the models present a noticeable long-term increase of temperature over the area. This increase of temperature appears larger than in the reanalysis for the BCC, HadGCM and CISRO models, and lower than in the reanalysis for ICHEC.

The quantification of the SHL trend in the reanalysis can be assessed from the unfiltered time series of three different quantiles (i.e. Q10, the median-i.e. Q50- and Q90) of the seasonal distribution of the SHL intensity (Fig. 4a). For the three members, we observe two stable periods in the 80s and 00s separated by a transitional period in the 90s with a temperature gradient of about 0.15 °C year$^{-1}$. Even if the inter-annual variability of these mean temperatures is large, the differences between the 80s and the 00s are significant, based on a 0.9 level of the Mann–Kendall-test (Mann 1945) for Q90 and the median. The lowest intensities (Q10) of the SHL appear to be more or less constant during the last 30 years. The significance of the trend in the 90s was tested using the Mann–Kendall test. The origin of this trend

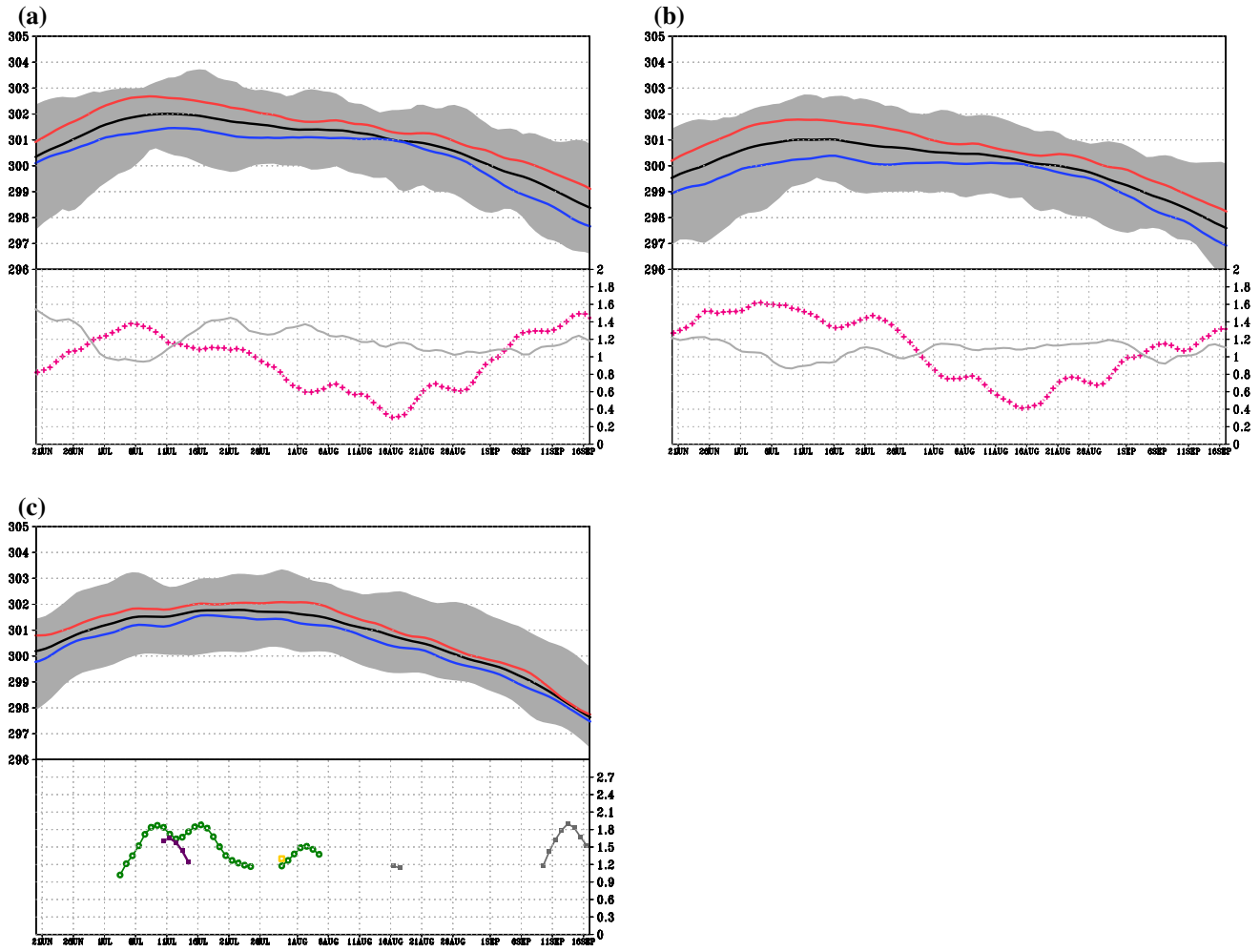


**Fig. 7** *Upper graphs* of each *panels*: daily mean (*black lines*) and standard deviation (*grey line filled*) of the heat low (in K) during the summer season for the 1979–2008 period using ERAI (**a**), and NCEP2 reanalysis (**b**). For each reanalysis, the mean seasonal cycle during the cold period (1979–1988) and the warm period (1999–2008) are indicated in *green* and *red* respectively. *Lower graphs* of each *panels* display the temperature difference between the warm and the cold season (in K, *purple lines*), the 0.9 significance level are indicated (*grey lines*). **c** Same as previously by using the 15 ensemble climate models. Only models (GFDL_180 in *grey*, HadGEM2 in *green*, INM in *yellow* and IPSLA in *purple*) and periods with significant difference are plotted

is discussed in Evan et al. (2015), and could be associated with a positive anomaly of humidity in low tropospheric layers over the Sahara.

The distribution of the SHL has then been decomposed in different periods of variability motivated by recent studies presented in the Sect. 1. The filters used are the high band pass level (define as a 1–25-day filtering), the 25–100-day filter, and the low band pass (defined as the signal filtered up to 300 days, Fig. 2b–d). The seasonal mean or yearly mean does not capture one of the most important characteristic of the SHL intensity during the season which is its intra-seasonal pulsations. For these reasons it is important to analyze the recent evolution of the pulsation of the SHL intensity.

At intra-seasonal scales (using the high band pass and the 25–100 day filtering, Fig. 2b, c for the entire distribution and Fig. 4b, c for three different members, i.e. Q10, Q50 and Q90), the evolutions are not related to the large trends observed in the unfiltered signals. The high band pass signal is associated with an increase of activity during the transitional period in the 90s for Q90 and the median, but compensated by a relative low Q10. In the 00s, the activity decreases. In addition, the seasonal variance of the filtered signals does not evolve significantly. This suggests there is no relation between the recent increase of the unfiltered SHL activity and the evolution of the intra seasonal pulsations.

As expected, the decadal-scale trend observed in the unfiltered signal is only found using the low-pass filter (Fig. 2d for the distribution and Fig. 4d for the three quantiles Q10, Q50 and Q90).

The climate models are now used as an ensemble system to evaluate the capacity of the ensemble of models to catch

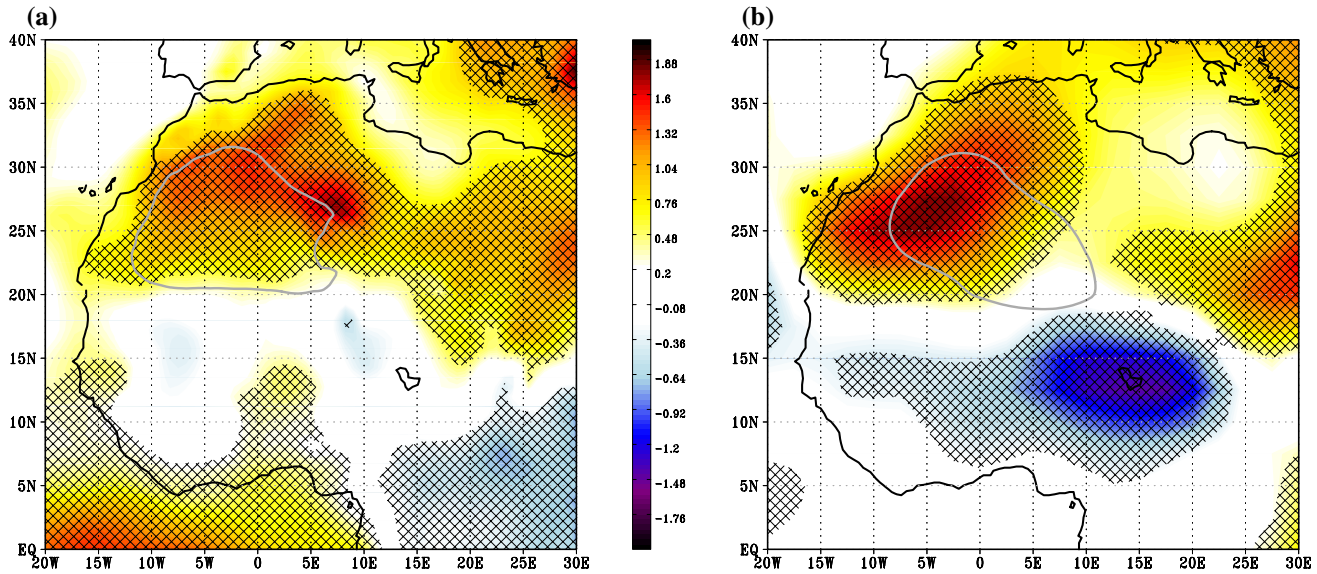


**Fig. 8** Difference between 00s and 80s of the 850 hPa temperature field using ERAI (in degree, *left panel*) and NCEP2 (*right panel*) reanalysis, hatched regions indicate results larger than the 0.9 significance level. The mean location of the SHL, defined as the 300 K level in the 850 hPa temperature, is indicated with the *grey contours*

the observed trends. Using the unfiltered signal (Fig. 5a), an acceleration of the warming is observed during the 90s (+0.05 deg/year) with respect to the increase of the 80s (+0.02 deg/year) and in the 00s (+0.03 deg/year). This means that the ensemble of the climatological models is able to reproduce the trends observed in the reanalysis (Fig. 4). This trend appears to be strongly related to a slight, long-term increase of the temperature. Indeed, the characteristics of the high-pass and band-pass filtered signals are constant in term of average and spread along the years (Fig. 5b, c) and, as shown using the reanalysis, the significant increase is associated with the median of SHL intensity filtered with the low-pass (Fig. 5d). For the unfiltered and filtered signals, the standard deviation of the SHL intensity is quite similar from 1 year to the other (black lines). As in the reanalyses, the change of the SHL characteristics in the climate models seems to be only associated with a slow increase of the SHL intensity (i.e. a small increase of temperature for every day during the summer seasons).

These results depict the recent increase of the temperature that is associated with a slow and long-term trend and with a very small modification of the intra-seasonal variabilities of the SHL. This is confirmed by the normalized frequency distributions of the unbiased intensity of the SHL in the 80s (from 1979 to 1988) and 00s (from 1999 to 2008, Fig. 6). The two distributions are close when the average of the decadal mean intensity of the SHL (assessed by the mean 850 hPa temperature within the SHL) is removed. The relative strongest SHL intensities are even reduced in ERAI. The biggest difference is the number of relative low SHL intensities in the 80s (blue doted line).

### 3.2 Temporal and spatial variabilities of the temperature trends

The recent trend of the SHL is now further analyzed using the 80s and 00s periods (corresponding to the 'cold' and the 'warm' SHL periods, respectively).

First the temporal variability is analyzed in Fig. 7. Due to the seasonal cycle of the solar radiation, the maximum of the SHL intensity occurs generally in the beginning of July. Rainfall events and cloud cover occurrence generate large inter-annual variability of the low level temperature (shaded area that can fluctuate from ±10 K). Based on these figures, the recent increase does not seem to be temporally homogeneous. We first note a significant increase of the SHL intensity during the beginning of the period (Fig. 7a), when the SHL is stronger (from 25 June to 15 July). This increase appears significant (bottom graph in Fig. 7a) and could be related to the modification of the rainy season discussed in Sighomnou et al. (2013) that show the increase of precipitation during this period. A second significant increase is observed at the end of the rainy season (end of August–beginning of September). Biasutti (2013) found modifications in the seasonal cycle of the Sahelian precipitation in the twentyfirst century, as a response to greenhouse gas forcing, observing a negative (positive) trend of precipitation in early (late) monsoonal season, whereas Cook and Vizy (2015) found no difference. The SHL intensity trends observed in both early and late monsoonal season suggest a significant modulation of the global forcing by the SHL regional signal. These two increases are also observed in the NCEP reanalysis during the same period (Fig. 7b).

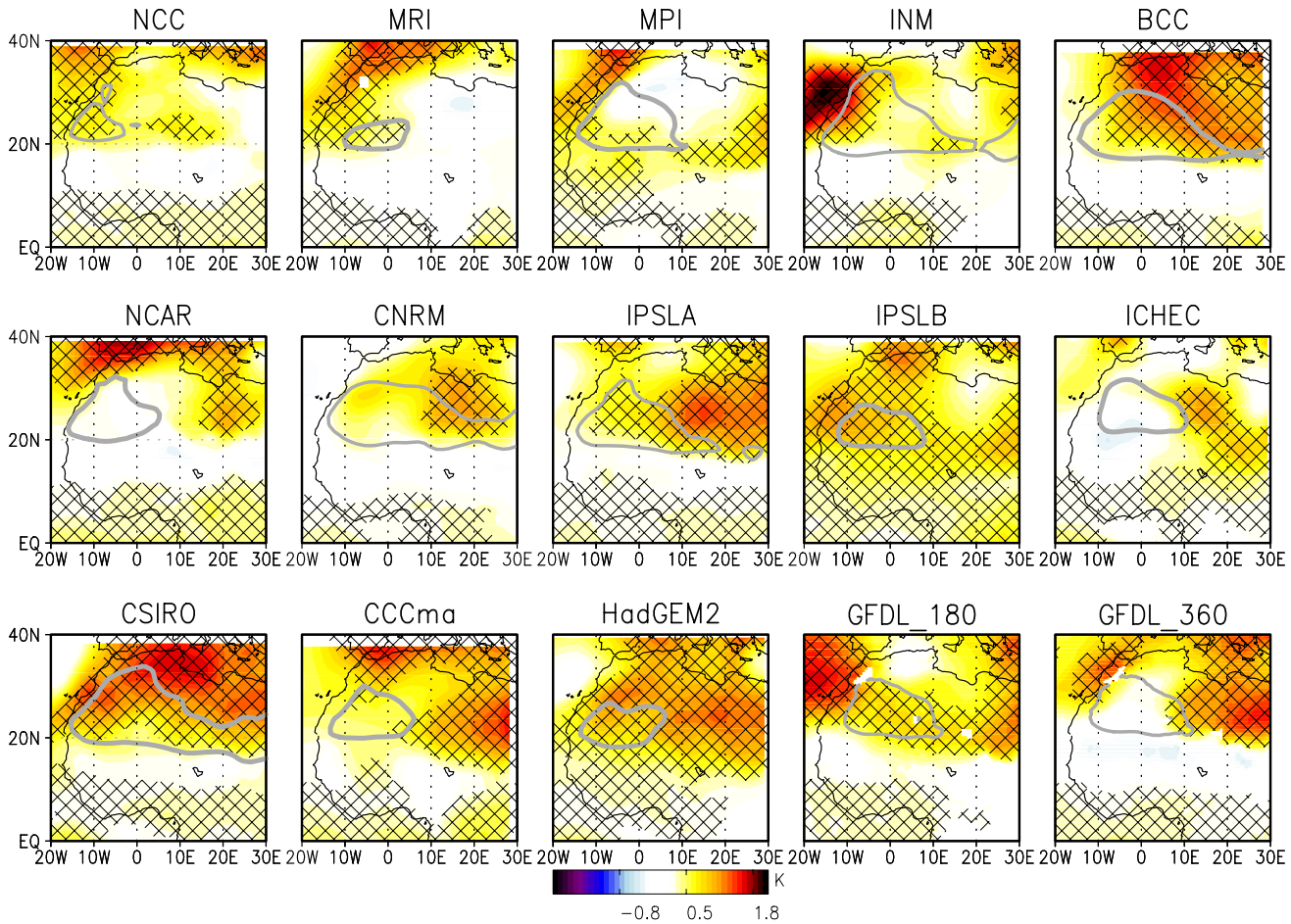


**Fig. 9** Difference of temperature at 850 hPa between 00s and 80s using different GCMs, *hatched regions* indicate results larger than the 0.9 significance level. The mean location of the SHL, defined as grid points where the temperature is larger than 300 K, is indicated in *gray contours*. The threshold has been determined using the reanalysis

Cook and Vizy (2015) assessed the increase of temperature based on a linear trend. However, it seems that the assumption of a linear trend is not well adapted because, during the 90s, the increase is stronger than the 80s or the 00s. For these reasons, we believe it is more relevant to compare temperature differences between the 80s and the 00s rather than assessing the temperature increase in the Sahara based on the linear trend derived from Cook and Vizy (2015).

The evolution of the SHL intensity is now discussed based on the ensemble of climate models (Fig. 7c). The mean seasonal cycle is in agreement with those obtained with the reanalysis. Nevertheless, the maximum of SHL intensity is slightly delayed in the middle of July. Due to cold or warm biases of the climate models, the ensemble spread associated with the ensemble mean dominates the inter-annual variability in the reanalysis. That is why, in Fig. 7c, the spread is calculated with respect to the mean of each individual model. Despite this change, we note a global increase of the temperature during the whole season. The daily differences are generally not significant with respect to the mean spread.

The spatial distribution of this increase is now studied in order to characterize the increase of the temperature inside the SHL in relationship with the surrounding areas. To address this, we compare the difference in the 850 hPa temperature between the 00s (averaged from 1999 to 2008) and the 80s (averaged 1979–1988, Fig. 8). These periods have been chosen based on the trend of the SHL intensity shown in Fig. 4d. Even though the two reanalyses both represent the positive trend of temperature inside the SHL region, differences can be observed. Using ERAI, the increase of temperature is located in the eastern part of the Sahara (Fig. 8a), whereas in the NCEP2, the maximum of increase is located more to the West (Fig. 8b). Also, in NCEP2 an area with significant negative temperature anomaly is found over the Eastern part of the Sahel area (around Lake Chad) that is not depicted using ERAI. These results show the uncertainties, even using the reanalyses, related to the spatial pattern of this temperature trend. Nevertheless, it is worth noting that even in a global warming environment, the SHL area is much more influenced by this warming that

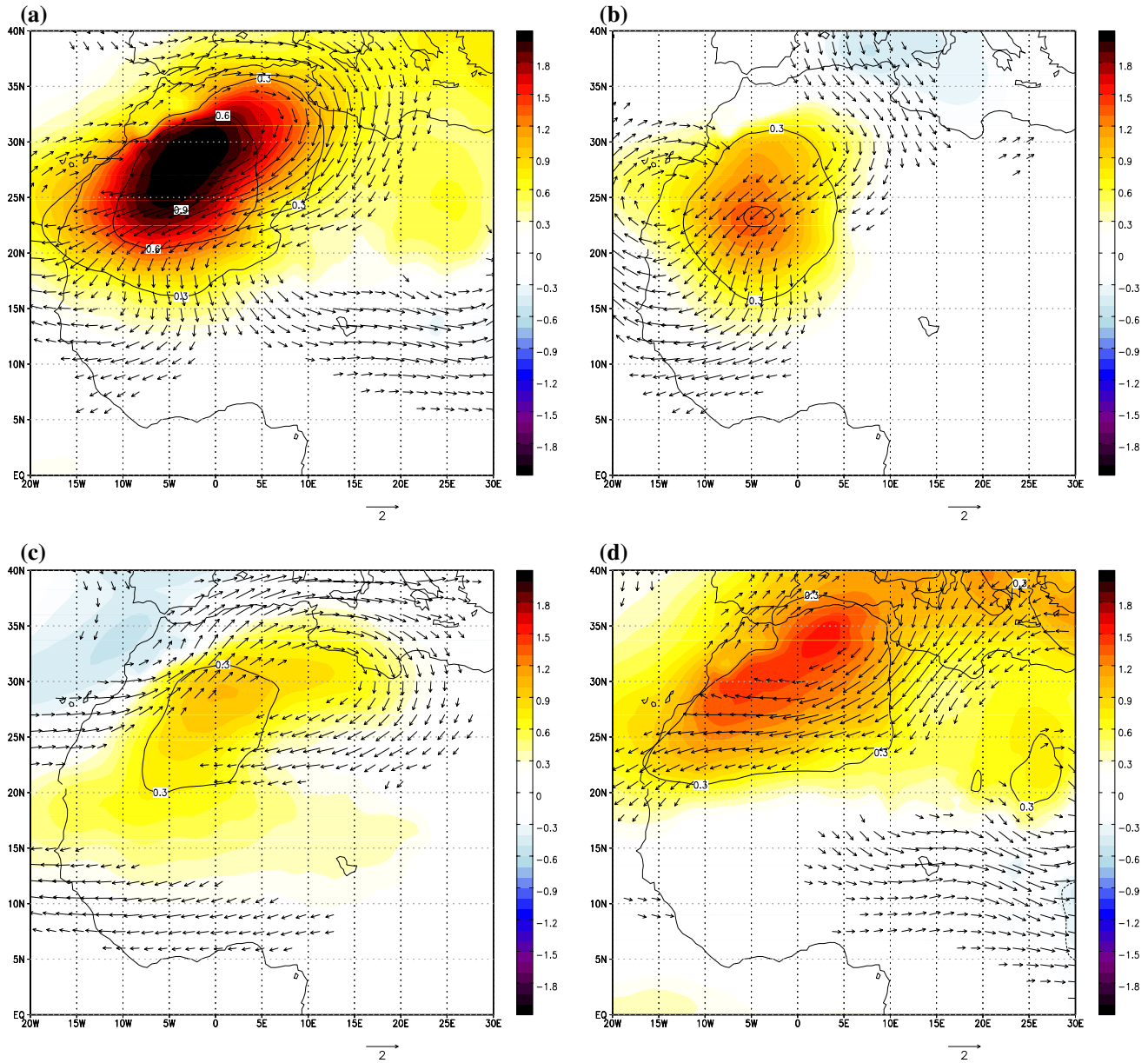


**Fig. 10** 2D regression analysis of temperature at 850 hPa (*shaded*, in K $K^{-1}$) and 700 hPa wind fields (in *vectors*, in m $s^{-1}$ $K^{-1}$) from ERAI. The regression is done by using as reference different signals from the SHL intensities: unfiltered data (**a**), high band pass filter (**b**), 25–100-day filter (**c**), and low band pass filter (**d**). Results are plotted only where the significance level of the regression is up to 0.9. The correlations are indicated in *thin contours*

the surrounding areas. In that context, the impacts of the SHL could be increased in West Africa.

Using the climate models, the position and the intensity of the maximum 850 hPa temperature allow to compare the location of the SHL during the summer season (grey contours in Fig. 9). Models with warm bias previously cited (INM, BCC, CNRM and CSIRO) exhibit a wider SHL area than the reanalysis. On the opposite, NCC and MRI show a very small area associated with the SHL. The position of the SHL is quite homogeneous for a large number of models. Nevertheless, the SHL position is significantly displaced to the West for NCC and NCAR. The spatial temperature trend in the climate models is also displayed in Fig. 9. Most models display an increase of temperature between 20 and 30°N. The location in longitude of this increase of temperature is highly variable, generally located either on the eastern or on the western edge of the SHL location. The intensities are also different, and a large number of the models underestimate the temperature differences between the 00s and the 80s with respect to the reanalyses. None of the 15 climate models used here produces an overestimation of the temperature increase over

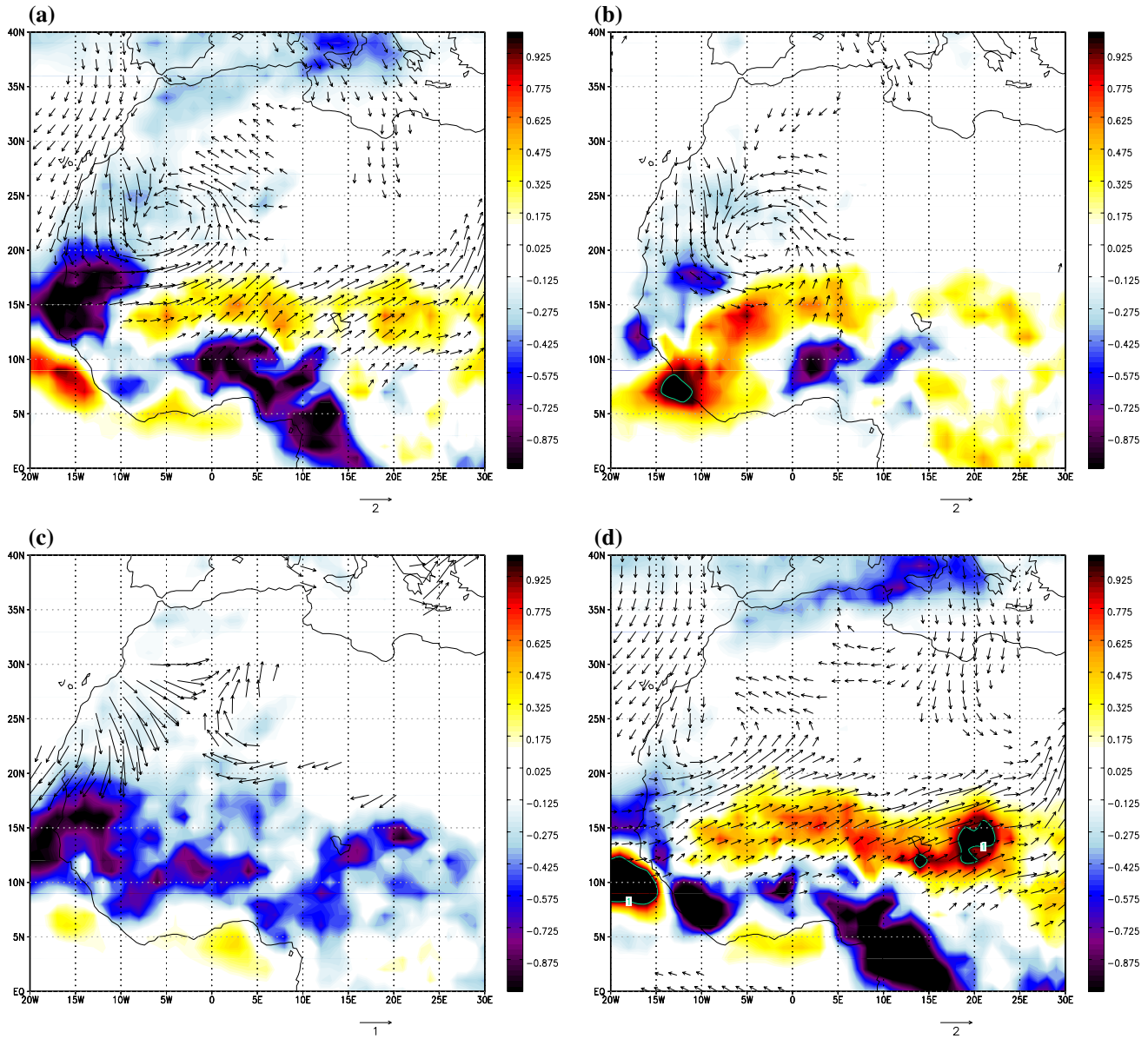


**Fig. 11** 2D regression analysis of precipitation from GPCP (*shaded*, in mm day$^{-1}$ K$^{-1}$) and wind fields (in *vectors*, in m s$^{-1}$ K$^{-1}$) at 925 hPa, from ERAI. The regression is done by using as reference different signals from the SHL intensities: unfiltered data (**a**), high band pass filter (**b**), 25–100-day filter (**c**), and low band pass filter (**d**). Results are plotted only where the significance level of the regression is up to 0.9

the Sahara between the two decades. This could partially explain the underestimation of the rainfall recovery in the climate models described in Evan et al. (2015). Several models seem to even miss the decadal trend over the Sahara (NCAR and ICHEC), whereas two of them (CSIRO and BCC) are in agreement in term of intensity, but with a wrong representation of the pattern. Finally, it is worth noting that twelve out of the 15 models agreed to conclude that the Sahel area (between around 12–20°N and −20 to 10°E) is not affected by a significant temperature increase. These results highlight the uncertainties of the climate models over the Sahara area and highlight that even if the mean of the climate models agreed on the global increase during the 90s, they are not in accordance regarding the location and the intensity of this trend. This is a key problem because the local impacts will be different regarding the spatial pattern of the trend.

### 3.3 Impact of the SHL pulsations

The impacts of the SHL pulsation at intra-seasonal timescales have been already studied in Lavaysse et al. (2010a)

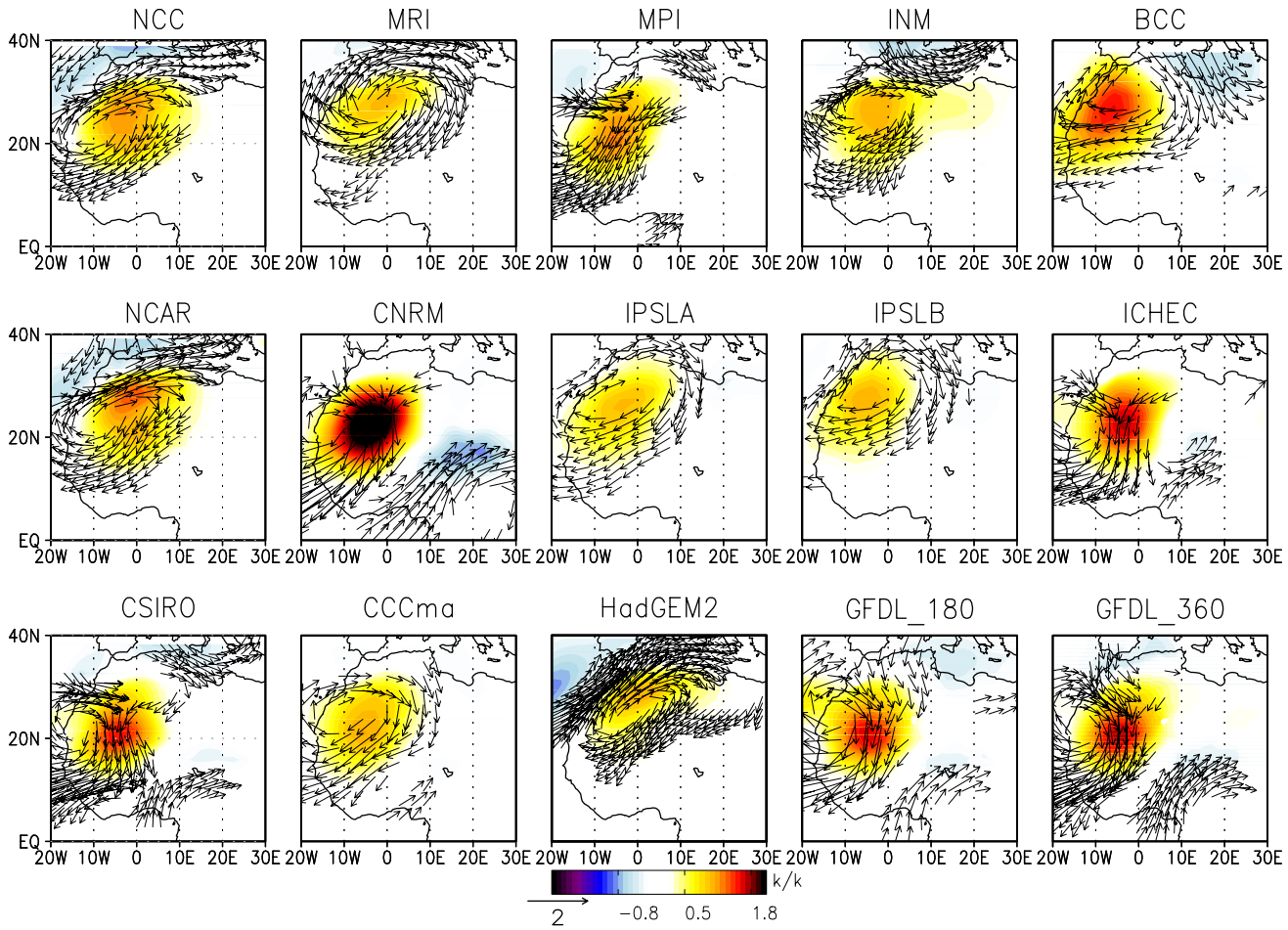


**Fig. 12** Regression analysis of temperature (*shaded*, in K $K^{-1}$) and wind at 700 hPa (*vectors*, in m $s^{-1}$ $K^{-1}$) based on the high band pass filtered SHL intensity for the 15 climate models for the period 1979–2008

and Roehrig et al. (2011). We now examine the impacts of the SHL pulsations at the different time scales (lower than 25 days, between 25 and 100 days and larger than 300 days) on the atmospheric circulations using the regression maps onto temperature, wind fields as well as precipitation.

The mechanisms associated with the SHL pulsations are analyzed using the 700 hPa wind fields which is generally used to describe processes at regional and synoptic scales (Fig. 10). The regression map based on the unfiltered SHL temperature displays a large scale anticyclonic circulation feature associated with the divergence on the top of the SHL (Fig. 10a). The increase of the SHL activity is depicted by a local intensification of temperature over the North-Western part of the Algeria. In the meantime, at 925 hPa, the intensification of the SHL temperature is associated with an increase of the cyclonic circulation in the Sahara. A large scale signal of wind appears significant over the entire Sahel area (around 15°N, Fig. 11a) and is associated with an increase of the south-westerly winds. The patterns of precipitation anomaly display both longitudinal and latitudinal dipoles centered over 12°N and 10°W and is in agreement with the wind fields: increase of the monsoon flow on the eastern part, increase of the northerly Harmattan wind on the Western part of the domain (located at 15°N and close to the Atlantic coast).

The impacts of the high band-pass filtered pulsations are located close to the location of the SHL center (Figs. 10b, 11b). The cyclonic circulation is well defined, and its impact on the wind circulation and precipitation is confined to the west of 10°E and to the South of 30°N. During the intensification period of the SHL, a shift of precipitation toward the north occurs east of 0°E. On the opposite, in the western part of the SHL (around 10°W), precipitation is enhanced to the south due to the intensification of the dry Harmattan wind.

The signal within the 25–100-day filtering band period (Figs. 10c, 11c) is relevant to capture the impact of MJO over West Africa. Mohino et al. (2011) have shown that around 15–20 days after the maximum increase of convection in the Indian Ocean, the precipitation decreases over

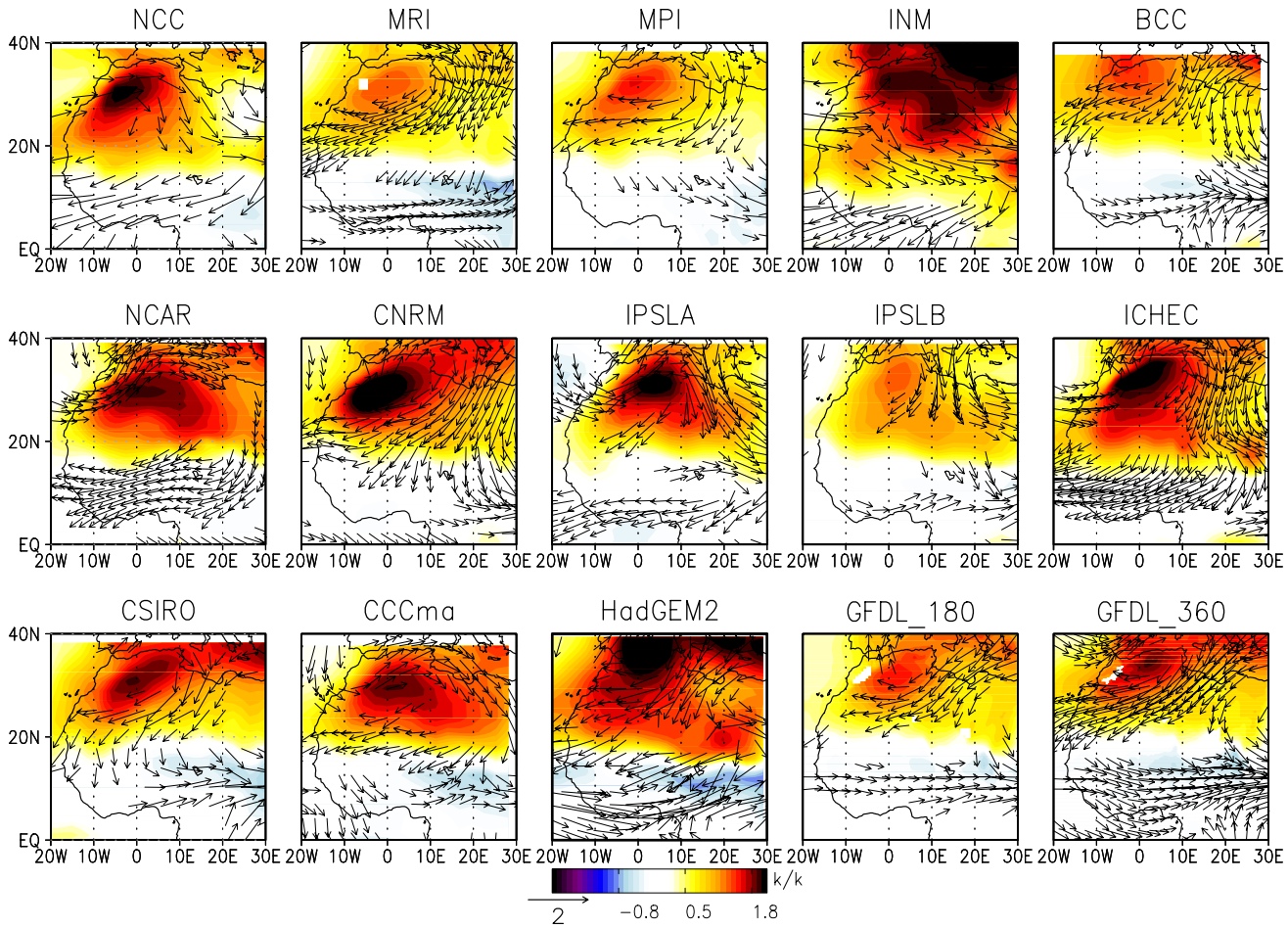


**Fig. 13** Same as Fig. 12, but using the low band pass filter (larger than 300 days) of the SHL intensity

West Africa. The impacts are seen over the entire southern part of West Africa, whereas a small increase of outgoing Long-wave Radiation (OLR) is seen over northern West Africa, in agreement with previous work, thereby suggesting that this band period is dominated by the MJO signal.

Associated with the large increase of temperature over the northern part of Algeria at seasonal time scales (Figs. 10d, 11d), the low-pass filtered 925 hPa wind field displays a northward shift of the ITCZ along the Sahel area at 10°N over the entire domain. The precipitation pattern shows a reduction of the precipitation over the Guinean coast. This is consistent with the seasonal migration of the ITCZ to the north in June and to the south in September.

Figures 10 and 11 allow us to unambiguously characterize the impacts of the SHL pulsations at different time scales as shown by the reanalyses. Note that ERAI is used here but very similar results have been found using the NCEP2 reanalyses (not shown). Interestingly, the modifications in the regional circulation in the lower troposphere, associated with the low frequency trend, are consistent with the response of the large scale atmospheric circulation to projected emission scenarios in the mid-twentyfirst century, as observed by Monerie et al. (2012, 2013). Specifically, they found a similar west-east Sahel precipitation dipole associated with more intense anticyclonic circulation over the subtropical Atlantic, reinforced northerly flow from the Mediterranean region and a strong westerly flow across the Sahel, related to a strengthened zonal circulation between Atlantic and Indian oceans.

As shown using the reanalyses, the impacts of the SHL pulsations are important to explain the main variability modes of precipitation. That is why the correct representation of the SHL pulsations and their impacts in climate models is important. This is helpful to identify processes well represented in the models at different time scale but also this can help identifying predictors of precipitation patterns that are better represented in the models than precipitation. The behaviour of the climate models is now checked with respect to the results found using the reanalysis. The same regression analyses have been done for the 15 climate models for the raw and filtered signals. Except for the HadGEM2 model (large overestimation of

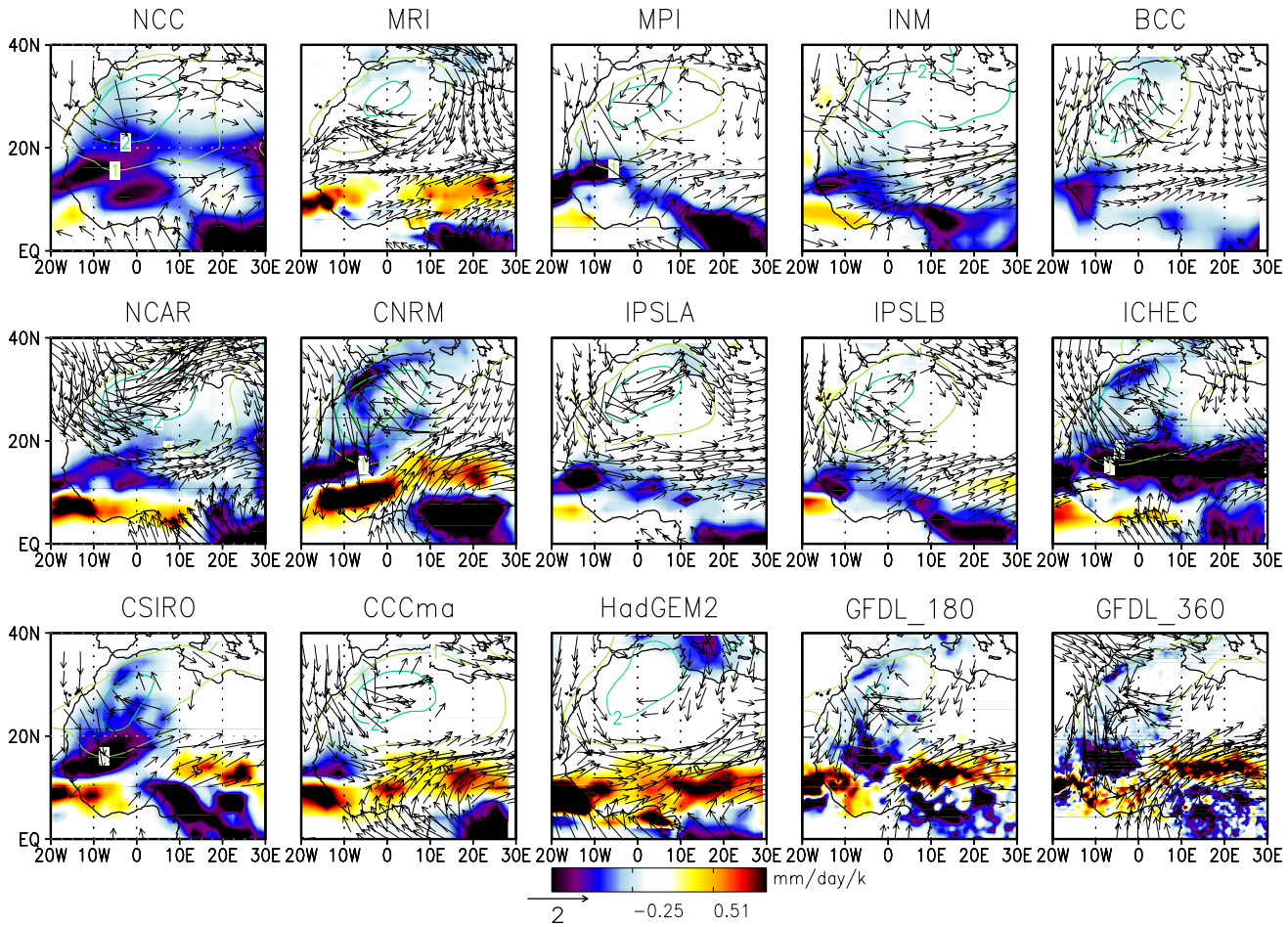


**Fig. 14** 2D regression analysis of precipitation (*shaded*, in mm day$^{-1}$ K$^{-1}$), 925 hPa wind field (in *vectors*, in m s$^{-1}$ K$^{-1}$) and 850 hPa temperature (*thin contours*, in K K$^{-1}$) from each of the 15 climate models. The regression is done by using as reference the unfiltered SHL intensities from each climate model independently. Only significant results above the 0.9 level are plotted

the temperature response and different wind field) and the INM model (overestimation of the temperature response), the regression map of wind and temperature in relationship with the evolution of the raw SHL is relatively well reproduced (not shown).

The regression map of the high band pass filtered signal is now analyzed in more details. The SHL pulsations at this time scale are known to be a large scale forcing for mesoscale convective systems and their impact on precipitation variability has been shown in the previous section and in recent studies (Lavaysse et al. 2010b). The results of the regression map for the high band pass filtered SHL intensity series is shown in Fig. 12, and should be compared to the regression map for the reanalyses provided in Fig. 11. For this mode of variability, except for the CNRM model that overestimates the temperature response in relationship to the reanalyses and HadGEM2 that represents the impacts too far to the north, the location and the intensity of the temperature response of the SHL pulsations appear in accordance with the results from reanalyses.

Despite this good agreement for the temperature, the impact in the wind field displays more uncertainties. The intensity, the location and the size of the anticyclonic circulation on top of the SHL are more uncertain. MRI, INM, BCC, IPSLA, IPSLB and HadGEM2 represent an anticyclonic circulation that is too much inland, with a position shifted toward the north-east. On the opposite, MPI, CNRM, ICHEC, CSIRO, CCCma and GFDL display a centre of rotation associated with the SHL in the right location. In that last group of models, there is a slight overestimation of the wind speed over the Sahara area for CNRM, ICHEC and GFDL that could be related to the overestimation of the temperature response.

For the low band pass (Fig. 13) and the 25–100-day filtered signals (not shown), a large majority of the climate models overestimates the response on the temperature and wind fields. This is particularly true for the INM and HadGEM2 models. For the majority of the models, the location is quite similar, with a maximum of temperature in the northern part of Algeria, along the western edge of the Atlas

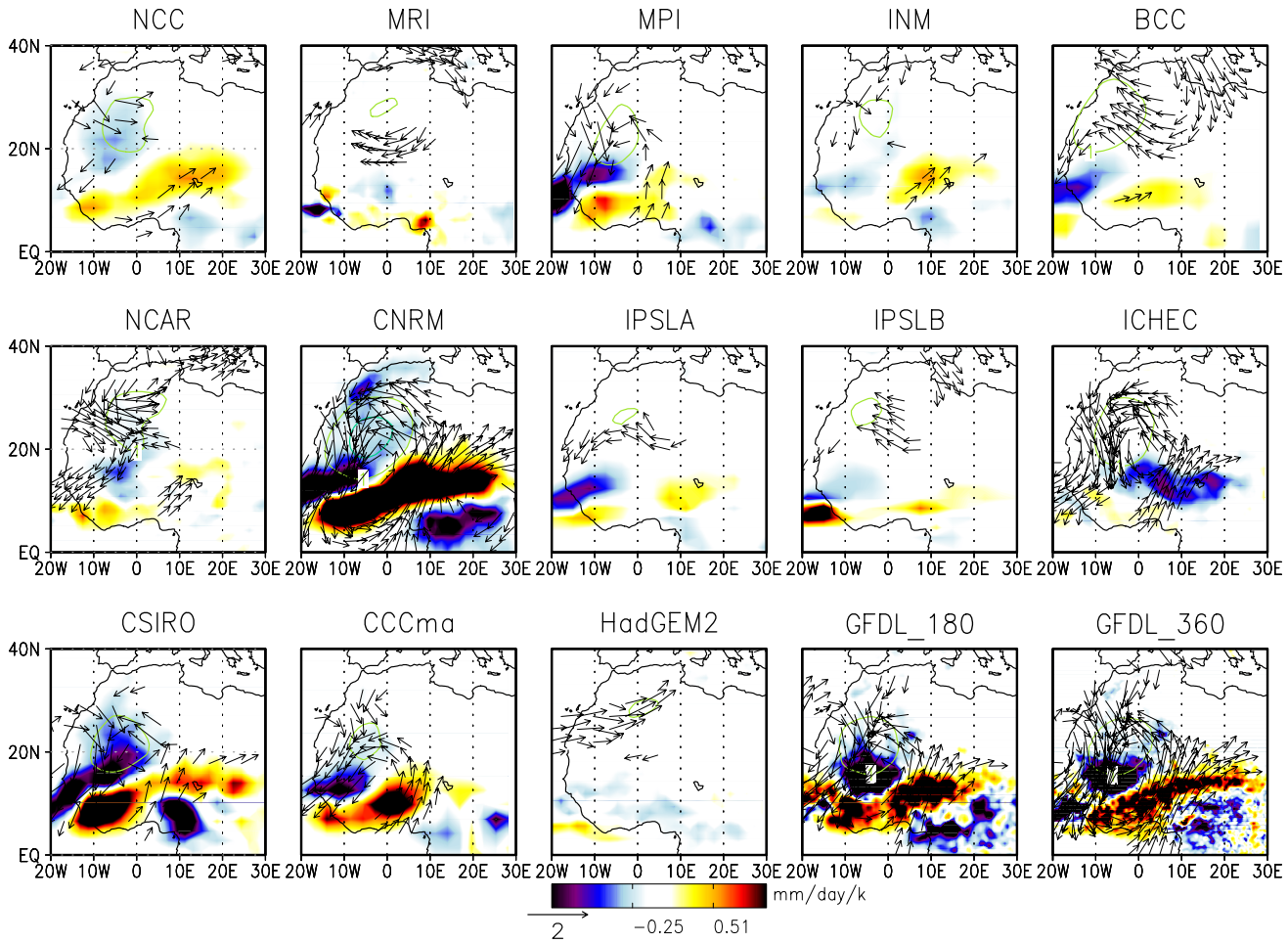


**Fig. 15** Same as Fig. 14 but using the high band pass filtered SHL intensity

chain. As observed for the low band pass filtered signal, the wind field responses are much more variable. Whereas MRI, MPI BCC, CNRM and CSIRO are in relatively good agreement with the reanalyses, the results from NCC, INM and HadGEM2 are very different. It is important to note the impact of the resolution change with GFDL both in terms of the intensity and the location of the impacts.

The same regression has been done to analyze the impact on the 925 hPa wind speed and precipitation. Note that it is not possible to combine here the observed precipitation and the variables of the climate models. Indeed, it is not the objective of these models to reproduce the exact events at the correct period. So to assess the quality of the representations of the impacts of the SHL pulsations in the climate models, we have used precipitation data from the climate models. Figure 14 highlights the impacts of the SHL pulsations onto the 925 wind fields and precipitation simulated by the climate models. These panels should be compared to the results from reanalysis in Fig. 11a. The regression of the 925 hPa wind fields allows to distinguish different behaviours. Except for NCC, INM, IPSLA and HadGEM2, a cyclonic circulation is found around the SHL center. Nevertheless, the location of this circulation can be slightly different to those obtained with the reanalyses. For example, the NCAR and CCMa models represent this circulation north to 35°N. Note that, some of them have a good agreement in terms of intensity and location of this low level circulation such as BCC, IPSLB and the two models of GFDL. In terms of precipitation, we can see the large uncertainties of the climate models to correctly represent the processes, based on the large differences of the regressions found. It is even possible to find opposite behaviours among models for which the regressions of the wind are not so different. For example, based on NCC and HadGEM2, the increase of the SHL intensity tends to increase the southerly component of the monsoon flow in the Sahel area, but surprisingly, in NCC the precipitation tend to decrease in the meantime. Using ICHEC, the same decrease of precipitation is observed but in that case, this is explained by the increase of the Harmattan wind. Note that CNRM, CSIRO, CCMA and the two models of GFDL are able to capture the complex structure of the precipitation

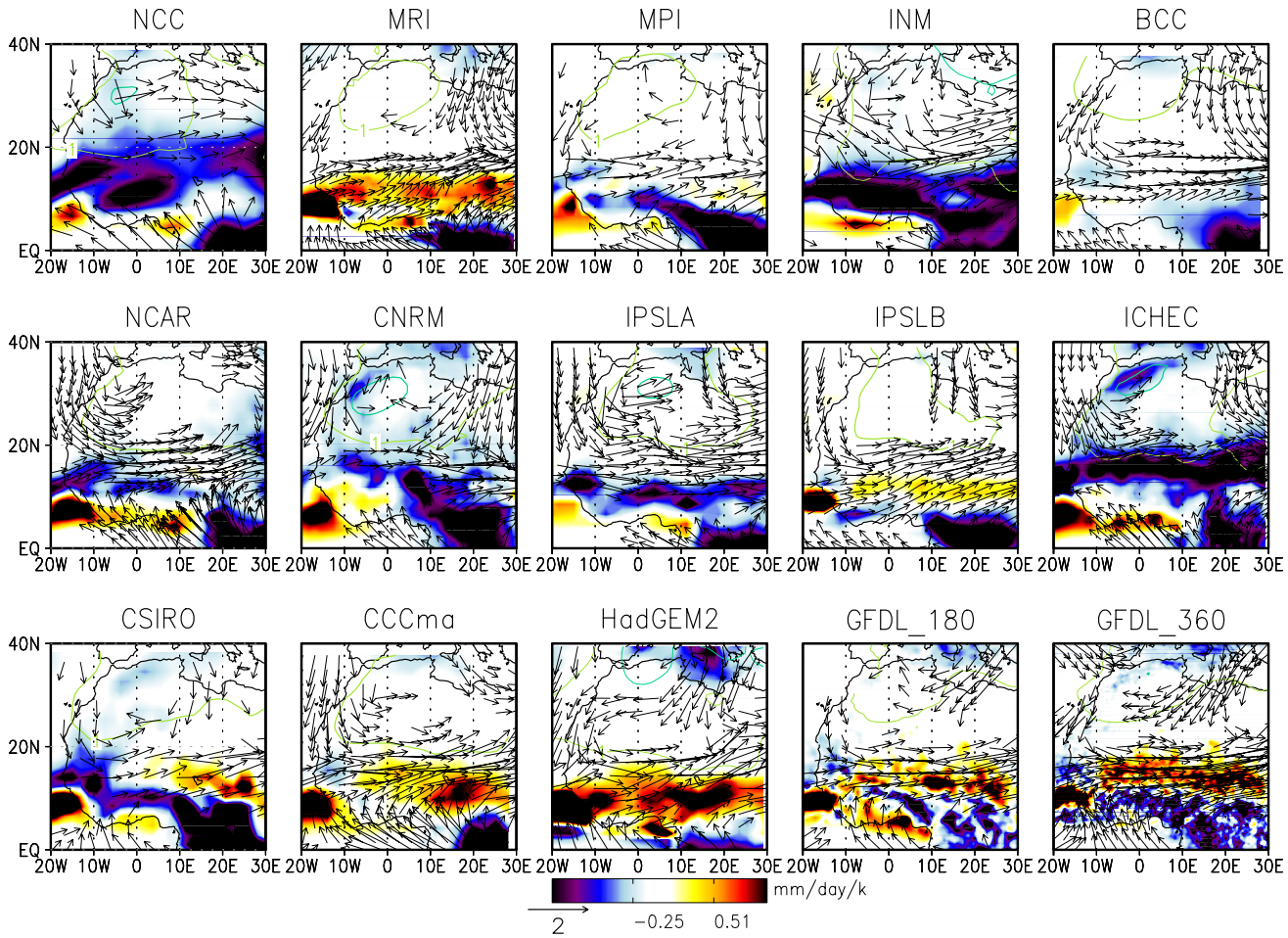


**Fig. 16** Same as Fig. 14 but using the low band pass filtered SHL intensity

observed in Fig. 11a with both latitudinal and longitudinal dipoles.

The regression using the decomposition onto the two most important band periods of the SHL pulsations have been done (Figs. 15, 16). With the high band pass filter (Fig. 15) and in comparison with results obtained using the observations and the reanalyses (Fig. 11b), we can first decompose two groups of model. The first group clearly underestimates the impacts of the SHL onto the 925 hPa wind speed and precipitation (NCC, MRI, INM, IPSLA, IPSLB and HadGEM2). For those models, the impacts of the 1–25-day filtered SHL are very low. On the opposite, the CNRM model overestimates the response of the SHL pulsations. Nevertheless, even if the intensities of the responses are overestimated, it is interesting to note that the patterns of the regression for both the wind fields and the precipitation are in accordance. The results obtained with ICHEC are difficult to interpret since the wind field depicts an increase of the monsoon flow over the Sahel, but the precipitation patterns depict a strong and significant decrease of precipitation during a strong SHL event. Finally, we can notice that CSIRO and the two models of GFDL are in accordance with the results obtained in Fig. 11b.

The second specific impact at interannual and interdecadal timescales is analysed. As we have seen previously (Fig. 5d), the ensemble system of the climate models is able to represent the long term increase of the SHL intensity from the 80s to the 00s. Here, the regression of the 925 and precipitation fields is analyzed to quantify the impact of this increase using the climate models (Fig. 16) and it will be compared to the results from the reanalyses (Fig. 5d). A first group of models displays a decrease of precipitation associated with the increase of the SHL intensity over the Sahel (NCC, INM, CNRM, IPSLA and ICHEC). This is the opposite result from the one obtained using the reanalyses as well as observations. For most of these models, the reasons of this decrease of precipitation are explained by an increase of the Harmattan, and the northerly component of the wind over the SHL area. This tends to decrease the moisture advection and precipitation over the Sahel.

In this group, the individual trends have been analyzed to ensure that the maximum of the SHL intensity occurs during

the 00s (not shown). We have seen that the trend toward the increase of the SHL activity is significant over the Sahara for INM, CNRM and IPSLA during the 00s in relationship with the 80s. For these models, the trend of the SHL is in agreement with the climatology but the models are not able to represent the mechanisms associated with this kind of mechanisms. This means also that these models appear less robust to represent the trend of the precipitation in the future over the Sahel. On the opposite, we note a good representation of the wind and precipitation fields for IPSLB, CSIRO, CCCma, and the two GFDL models. Except for GFDL_360, the models are also in agreement with the long term evolution of the SHL intensity (Figs. 3, 9).

## 4 Conclusion

The main objectives of this study were to characterize and compare the trend of the SHL intensity during the last 30 years, based on numerical weather prediction models reanalyses as well as AMIP simulations from 15 climate models. For that purpose, a decomposition into the main modes of variability of the SHL intensity has been done using different time filters. The impacts of these modes on key WAM features in the climate models have been compared with those obtained using the ECMWF and NCEP reanalyses.

In this study, we have shown that the recent increase of temperature is larger in the SHL area than in the surrounding regions. Moreover, specific modifications are observed in the SHL seasonal cycle and in the associated atmospheric circulation, in the context of large scale and regional changes related to global forcing. This result highlights the specificity of the SHL region and the potential increase of its influence on the WAM system by increasing the temperature gradient between the Gulf of Guinea and the Sahara. The ensemble mean of the climate models is able to represent the recent trend of the SHL observed in the reanalysis over the West Africa and more precisely the local enhancement over the SHL area. In both reanalyses and climate models, the recent increase of the SHL intensity is not associated with a change of the intra-seasonal pulsations of the SHL, meaning that this increase is associated with a slow and global increase of temperature. This has been highlighted by the fact that similar distributions of the unbiased temperature of the SHL are found during the two extreme periods of the SHL activities (namely, strong and weak SHLs).

Finally, the ability of the climate models to represent the mechanisms and the impacts associated with the SHL pulsations varies significantly depending on the mode of variability and the variable impacted. Based on the present study, a selection of the most adequate climate models was made as a function of the relevant time scales involved. This is especially important for future work to be conducted with climate models projections. A ranking of the climate models was performed based on the following SHL metrics: location, mean intensity, global trends, intra seasonal pulsations, impact on the WAM dynamic. It appears that three models (BCC, MPI and GFDL_180) are slightly better to represent the variabilities of the SHL intensity and its trend over the last 30 years. Regarding the impact of the SHL on the WAM, and more specifically the precipitation, the spread of the responses from the climate models is increased. At intra-seasonal time scales, we recommend to use MPI, CNRM (with an over estimation of the impacts), CSIRO and GFDL, whereas for the long-term evolution, MRI, IPSLB, CCCma and GFDL are recommended.

Of course, these suggestions are based on the relationship between the monsoon circulation and the pulsations of the SHL. This selection could be done based on other relationships between the WAM and synoptic or global pulsations, such as the African Easterly Waves, MJO or Rossby waves. This is primordial to evaluate the mechanisms that modulate the precipitation in the climate models in order to enhance our comprehension of the CIMP5 projections.

**Acknowledgments** We acknowledge the World Climate Research Programme's Working Group on Coupled Modelling which is responsible for CMIP, and we thank the climate modeling groups (listed in Table 1 of the paper) for producing and making available their model output. For CMIP, the U.S. Department of Energy's Program for Climate Model Diagnosis and Intercomparison provides coordinating support and led development of software infrastructure in partnership with the Global Organization for Earth System Science Portals. The authors also acknowledge the thoughtful comments of the two anonymous reviewer, which clearly helped to clarify and improve the manuscript.



## References

Biasutti M (2013) Forced Sahel rainfall trends in the CMIP5 archive. J Geophys Res Atmos 118:1613–1623. doi:10.1002/jgrd.50206

Chauvin F, Roehrig R, Lafore JP (2010) Intraseasonal variability of the Saharan heat low and its link with midlatitudes. J Clim 23(10):2544–2561

Collins WJ, Bellouin N, Doutriaux-Boucher M, Gedney N, Hinton T, Jones CD et al (2008) Evaluation of the HadGEM2 model. Hadley Centre Technical Note, 74

Cook KH, Vizy EK (2015) Detection and analysis of an amplified warming of the Sahara desert. J Clim 28:6560–6580. doi:10.1175/JCLI-D-14-00230.1

Dee DP, Uppala SM, Simmons AJ, Berrisford P, Poli P, Kobayashi S et al (2011) The ERA-Interim reanalysis: configuration and performance of the data assimilation system. Q J R Meteorol Soc 137(656):553–597

Donner LJ, Wyman BL, Hemler RS, Horowitz LW, Ming Y, Zhao M et al (2011) The dynamical core, physical parameterizations, and basic simulation characteristics of the atmospheric component AM3 of the GFDL global coupled model CM3. J Clim 24(13):3484–3519

Dufresne JL, Foujols MA, Denvil S, Caubel A, Marti O, Aumont O et al (2013) Climate change projections using the IPSL-CM5 Earth system model: from CMIP3 to CMIP5. Clim Dyn 40(9–10):2123–2165

Evan AT, Flamant C, Lavaysse C, Kocha C, Saci A (2015) Water vapour over the Sahara desert and drought in the Sahel. J Clim 28:108–123

Hazeleger W, Severijns C, Semmler T, Stefanescu S, Yang S, Wang X et al (2010) EC-Earth: a seamless Earth-system prediction approach in action. Bull Am Meteorol Soc 91(10):1357–1363

Huffman GJ, Adler RF, Morrissey MM, Bolvin DT, Curtis S, Joyce R, McGavock B, Susskind J (2001) Global precipitation at one-degree daily resolution from multisatellite observations. J Hydrometeorol 2(1):36–50

Janicot S, Mounier F, Hall NM, Leroux S, Sultan B, Kiladis GN (2009) Dynamics of the West African monsoon. Part IV: analysis of 25–90-day variability of convection and the role of the Indian monsoon. J Clim 22(6):1541–1565

Janicot S, Caniaux G, Chauvin F, De Coëtlogon G, Fontaine B, Hall N et al (2011) Intraseasonal variability of the West African monsoon. Atmos Sci Lett 12(1):58–66

Kalnay E, Kanamitsu M, Kistler R, Collins W, Deaven D, Gandin L et al (1996) The NCEP/NCAR 40-year reanalysis project. Bull Am Meteorol Soc 77(3):437–471

Kirkevåg A, Iversen T, Seland Ø, Debernard JB, Storelvmo T, Kristjánsson JE (2008) Aerosol–cloud–climate interactions in the climate model CAM-Oslo. Tellus A 60(3):492–512

Lavaysse C (2015) Warming trends: Saharan desert warming. Nat Clim Change 5(9):807–808

Lavaysse C, Flamant C, Janicot S, Parker DJ, Lafore JP, Sultan B, Pelon J (2009) Seasonal evolution of the West African heat low: a climatological perspective. Clim Dyn 33(2–3):313–330

Lavaysse C, Flamant C, Janicot S (2010a) Regional-scale convection patterns during strong and weak phases of the Saharan heat low. Atmos Sci Lett 11(4):255–264

Lavaysse C, Flamant C, Janicot S, Knippertz P (2010b) Links between African easterly waves, midlatitude circulation and intraseasonal pulsations of the West African heat low. Q J R Meteorol Soc 136(S1):141–158

Lee JY, Wang B (2014) Future change of global monsoon in the CMIP5. Clim Dyn 42(1–2):101–119

Li H, Wang H, Yin Y (2012) Interdecadal variation of the West African summer monsoon during 1979–2010 and associated variability. Clim Dyn 39(12):2883–2894

Lu J, Delworth TL (2005) Oceanic forcing of the late 20th century Sahel drought. Geophys Res Lett 32:1–5. doi:10.1029/2005GL023316

Mann HB (1945) Non-parametric tests against trend. Econometrica 13:163–171

Matthews AJ (2004) Intraseasonal variability over tropical Africa during northern summer. J Clim 17(12):2427–2440

Mizuta R, Yoshimura H, Murakami H, Matsueda M, Endo H, Ose T et al (2012) Climate simulations using MRI-AGCM3. 2 with 20-km grid. J Meteorol Soc Jpn 90:233–258 (Vol 2 num)

Mohino E, Janicot S, Bader J (2011) Sahel rainfall and decadal to multi-decadal sea surface temperature variability. Clim Dyn 37:419–440. doi:10.1007/s00382-010-0867-2

Mohino E, Janicot S, Douville H, Li LZ (2012) Impact of the Indian part of the summer MJO on West Africa using nudged climate simulations. Clim Dyn 38(11–12):2319–2334

Monerie PA, Fontaine B, Roucou P (2012) Expected future changes in the African monsoon between 2030 and 2070 using some CMIP3 and CMIP5 models under a medium-low RCP scenario. J Geophys Res Atmos 117(D16):1984–2012

Monerie PA, Roucou P, Fontaine B (2013) Mid-century effects of climate change on African monsoon dynamics using the A1B emission scenario. Int J Climatol 33:881–896. doi:10.1002/joc.3476

Mounier F, Janicot S, Kiladis GN (2008) The West African monsoon dynamics. Part III: the quasi-biweekly zonal dipole. J Clim 21(9):1911–1928

Neale RB, Richter J, Park S, Lauritzen PH, Vavrus SJ, Rasch PJ, Zhang M (2013) The mean climate of the Community Atmosphere Model (CAM4) in forced SST and fully coupled experiments. J Clim 26(14):5150–5168

Nicholson SE, Some B, McCollum J, Nelkin E, Klotter D, Berte Y et al (2003) Validation of TRMM and other rainfall estimates with a high-density gauge data set for West Africa. Part I: validation of GPCC rainfall product and pre-TRMM satellite and blended products. J Appl Meteorol 42(10):1337–1354

Parker DJ, Burton RR, Diongue-Niang A, Ellis RJ, Felton M, Taylor CM, Thorncroft CD, Bessemoulin P, Tompkins AM (2005) The diurnal cycle of the West African monsoon circulation. Q J R Meteorol Soc 131(611):2839–2860

Peyrillé P, Lafore JP (2007) An idealized two-dimensional framework to study the West African monsoon. Part II: large-scale advection and the diurnal cycle. J Atmos Sci 64(8):2783–2803

Roehrig R, Chauvin F, Lafore JP (2011) 10–25-day intraseasonal variability of convection over the Sahel: a role of the Saharan heat low and midlatitudes. J Clim 24(22):5863–5878

Roehrig R, Bouniol D, Guichard F, Hourdin F, Redelsperger JL (2013) The present and future of the West African monsoon: a process-oriented assessment of CMIP5 simulations along the AMMA transect. J Clim 26(17):6471–6505

Rotstayn LD, Collier MA, Dix MR, Feng Y, Gordon HB, O'Farrell SP, Smith IN, Syktus J (2010) Improved simulation of Australian climate and ENSO-related rainfall variability in a global climate model with an interactive aerosol treatment. Int J Climatol 30(7):1067–1088

Sighomnou D, Descroix L, Genthon P, Mahé G, Moussa IB, Gautier E et al (2013) La crue de 2012 à Niamey: un paroxysme du paradoxe du Sahel? Sci Chang Planét Sécheresse 24(1):3–13

Sultan B, Janicot S (2003) The West African monsoon dynamics. Part II: the "preonset" and "onset" of the summer monsoon. J Clim 16(21):3407–3427

Taylor KE, Stouffer RJ, Meehl GA (2012) An overview of CMIP5 and the experiment design. Bull Am Meteorol Soc 93(4):485–498

Thorncroft CD, Blackburn M (1999) Maintenance of the African easterly jet. Q J R Meteorol Soc 125(555):763–786

Ting M, Kushnir Y, Seager R, Li C (2009) Forced and internal twentieth-century SST trends in the North Atlantic. J Clim 22:1469–1481. doi:10.1175/2008JCLI2561.1

Villamayor J, Mohino E (2015) Robust Sahel drought due to the interdecadal Pacific oscillation in CMIP5 simulations. Geophys Res Lett. doi:10.1002/2014GL062473

Vizy EK, Cook KH, Crétat J, Neupane N (2013) Projections of a wetter Sahel in the twenty-first century from global and regional models. J Clim 26(13):4664–4687

Voldoire A, Sanchez-Gomez E, y Mélia DS, Decharme B, Cassou C, Sénési S et al (2013) The CNRM-CM5. 1 Global climate model: description and basic evaluation. Clim Dyn 40(9–10):2091–2121

Volodin EM, Dianskii NA, Gusev AV (2010) Simulating present-day climate with the INMCM4. 0 Coupled model of the atmospheric and oceanic general circulations. Izv Atmos Ocean Phys 46(4):414–431

Wu T, Yu R, Zhang F, Wang Z, Dong M, Wang L, Jin X, Chen D, Li L (2010) The Beijing Climate Center atmospheric general circulation model: description and its performance for the present-day climate. Clim Dyn 34(1):123–147